Proteasome Inhibition Enhances Lysosome-mediated Targeted Protein Degradation

Ahmed M. Elshazly[1,2,3], Nayyerehalsadat Hosseini[1], Janakiram Vangala[1], Shanwei Shen[1], Victoria Neely[4], Xiaoyan Hu[6,7], Piyusha P. Pagare[5] , Hisashi Harada[4,7], Steven Grant[6,7], Senthil K. Radhakrishnan[1,7*]

[1]Department of Pathology,
Virginia Commonwealth University, Richmond, Virginia, USA

[2]Department of Pharmacology and Toxicology,
Virginia Commonwealth University, Richmond, Virginia, USA

[3]Department of Pharmacology and Toxicology,
Faculty of Pharmacy, Kafrelsheikh University, Kafrelsheikh, Egypt

[4]Philips Institute for Oral Health Research, School of Dentistry,
Virginia Commonwealth University, Richmond, Virginia, USA

[5]Department of Medicinal Chemistry, School of Pharmacy,
Virginia Commonwealth University, Richmond, USA

[6]Division of Hematology and Oncology, Department of Internal Medicine,
Virginia Commonwealth University, Richmond, Virginia, USA

[7]Massey Comprehensive Cancer Center,
Virginia Commonwealth University, Richmond, Virginia, USA

Running Title: Lysosome-mediated Targeted Protein Degradation (TPD)

Keywords: AUTAC, TPD, proteasome inhibitor, NRF1, NFE2L1, Mcl1, cancer

*Correspondence:
Senthil K. Radhakrishnan
Senthil.Radhakrishnan@vcuhealth.org

ABSTRACT

Proteasome inhibitor drugs are currently used in the clinic to treat multiple myeloma and mantle cell lymphoma. These inhibitors cause accumulation of undegraded proteins, thus inducing proteotoxic stress and consequent cell death. However, cancer cells counteract this effect by activating an adaptive response through the transcription factor Nuclear factor erythroid 2-related factor 1 (NRF1, also known as NFE2L1). NRF1 induces transcriptional upregulation of proteasome and autophagy/lysosomal genes, thereby reducing proteotoxic stress and diminishing the effectiveness of proteasome inhibition. While suppressing this protective autophagy response is one potential strategy, here we investigated whether this heightened autophagy could instead be leveraged therapeutically. To this end, we designed an autophagy-targeting chimera (AUTAC) compound to selectively degrade the anti-apoptotic protein Mcl1 via the lysosome. Our results show that this lysosome-mediated targeted degradation is significantly amplified in the presence of proteasome inhibition, in a NRF1-dependent manner. Mechanistically, AUTAC-driven Mcl1 clearance requires K63-linked ubiquitination by UBC13 and TRAF6 and recognition by the cargo receptor p62/SQSTM1. The combination of the proteasome inhibitor carfilzomib and Mcl1 AUTAC synergistically promoted cell death in both in vitro models, including wild-type and proteasome inhibitor-resistant multiple myeloma and lung cancer cells, and in mouse tumor xenografts. Thus, our work offers a novel strategy for enhancing proteasome inhibitor efficacy by exploiting the adaptive autophagy response. More broadly, our study establishes a framework for amplifying lysosome-mediated targeted protein degradation, with potential applications in cancer therapeutics and beyond.

INTRODUCTION

Proteasome inhibitors (PIs) are a cornerstone in the treatment of multiple myeloma and are also part of mantle cell lymphoma therapeutic protocols [1,2]. FDA-approved PIs bortezomib, carfilzomib, and ixazomib are small-molecule inhibitors designed to target the proteasome. Bortezomib and ixazomib are peptide boronate inhibitors, mimicking proteasome substrates through dipeptide-like structures, while carfilzomib is an epoxyketone-based inhibitor that binds irreversibly to the β5 subunit [3]. By blocking proteasomal activity, these drugs induce endoplasmic reticulum (ER) stress due to the accumulation of unfolded proteins and insoluble aggregates, which ultimately leads to cell cycle arrest, activation of antiproliferative signals, and apoptosis [1,4,5]. While PIs have demonstrated clinical success in blood malignancies, they have shown limited efficacy against solid tumors [6-11]. Additionally, their long-term utility is often hindered by the development of resistance, leading to relapse and poor prognosis [12].

Tumor cells activate a range of adaptive mechanisms to counteract the cytotoxic effects of PIs, including the activation of nuclear factor erythroid 2-related factor 1 (NRF1, also known as NFE2L1). NRF1 resides in the ER membrane as an inactive p120 precursor and is cleaved by the protease DDI2 to its active p110 form upon proteasome inhibition. The active NRF1 translocates to the nucleus, where it upregulates the expression of proteasome and autophagy/lysosomal genes, thereby mitigating proteotoxic stress and reducing PI efficacy [13-15]. Although directly targeting NRF1 remains challenging due to the complexity of its pathway, adaptive responses such as NRF1-mediated autophagy induction could represent potential therapeutic vulnerabilities. Autophagy, a cytoplasmic recycling process critical for maintaining cellular homeostasis, enables tumor cells to survive under chemotherapeutic stress - a phenomenon referred to as cytoprotective autophagy [16,17]. Multiple studies have linked autophagy activation to PI resistance development [18-21]. Instead of inhibiting autophagy, here we sought to exploit this cytoprotective mechanism for therapeutic benefit using autophagy-targeting chimera (AUTAC) technology. AUTACs rely on cGMP-mediated S-guanylation, which has been implicated in the selective autophagic degradation of Group A Streptococcus (GAS) [22]. These compounds consist of an autophagy degradation tag, typically fluorobenzyl guanine (FBnG) derivatives, linked to a ligand that targets a specific protein of interest [23].

The anti-apoptotic protein Mcl1, a key regulator of mitochondrial integrity, binds and sequesters pro-apoptotic proteins such as Bax, Bak, and Bok, thereby preventing cytochrome C release and apoptosis [24,25]. Elevated Mcl1 levels following proteasome inhibition contribute to PI resistance in multiple myeloma [26-28]. Preclinical studies have shown that suppressing Mcl1 restores PI sensitivity [27,29-32], and several clinical trials are underway to evaluate Mcl1 inhibitors in multiple myeloma (NCT04178902, NCT03465540, NCT04543305, NCT02675452, NCT02992483). However, these efforts are constrained by concerns over potential cardiac toxicity [33].

In this study, we developed an AUTAC compound to selectively degrade Mcl1 via the lysosomal pathway. Our results demonstrate that this lysosome-mediated targeted degradation is significantly enhanced by proteasome inhibition in an NRF1-dependent manner. The combination of carfilzomib and Mcl1 AUTAC synergistically induced cell death in both wild-

type and PI-resistant multiple myeloma and non-small cell lung cancer cells. Importantly, AUTAC-mediated potentiation of carfilzomib cytotoxicity was further validated in a mouse xenograft tumor model, where the combination treatment resulted in significantly enhanced antitumor efficacy compared with either agent alone. Overall, our findings provide a novel strategy to enhance PI efficacy by leveraging the adaptive autophagy response.

RESULTS

AUTAC-Mediated Degradation of Mcl1 via Autophagic Machinery

Building on the efforts of Arimoto's group [22,23,34] and recognizing the importance of targeting Mcl1, we developed an Mcl1-targeting AUTAC utilizing a second-generation pyrazole-linked FBnG tag. This tag was conjugated via a pyrazole linker to the S1-6 derivative, a well-characterized Mcl1 inhibitor [35] (Fig. 1A). Sequence alignment revealed moderate overall conservation between Mcl1 and Bcl2 (33% identity, 50% similarity) and between Mcl1 and Bclxl (29% identity, 44% similarity), with notable divergence localized near the periphery of the BH3-binding groove (Supplementary Fig. 1A and B). These differences suggested that local surface topology at the groove entrance might influence accommodation of the AUTAC linker and degradation tag. To investigate this possibility, molecular docking studies were performed using Schrödinger's Glide module [36,37]. Crystal structures of Mcl1 (PDB ID 6YBL[38]), Bcl2 (PDB ID 2XA0 [39]), and Bclxl (PDB ID 1R2D [40]) were prepared using standard protocols, and the isolated warhead was first docked to establish a common binding framework. In all three proteins, the warhead adopted a conserved pose within the canonical BH3-binding groove (Supplementary Fig. 1C), consistent with the known BH3-mimetic ligand binding modes [41,42]. Importantly, the orientation of the linker exit position was preserved across targets, indicating that any differences in degradation are unlikely to arise from impaired warhead engagement.

AUTAC docking was then carried out using a core-constrained protocol to maintain the validated warhead pose while allowing flexibility of the linker and FBnG degradation tag. Across all three proteins, clustering analysis revealed a dominant binding family that differed primarily in linker trajectory and FBnG positioning at the groove periphery (Fig. 1B). Docking scores favored Mcl1 (top GlideScore −10.74) over Bcl2 (−7.10) and Bclxl (−7.13), despite identical warhead constraints, suggesting that selectivity arises from differential accommodation of the bifunctional architecture rather than intrinsic warhead affinity. Structural inspection revealed clear topological differences at the groove entrance. In the Mcl1 complex, the PEG linker extended along a shallow, solvent-exposed surface channel, positioning the FBnG tag away from the protein surface and largely accessible to solvent (Fig. 1B). In contrast, both Bcl2 and Bclxl presented more concave and restrictive surface contours, causing the linker to pack tightly against the protein and directing the FBnG tag into recessed surface regions near the groove entrance (Fig. 1B). These geometries suggest that Mcl1 uniquely supports productive presentation of the degradation tag.

To further quantify these differences, the top five docking poses for each target were subjected to Prime MM-GBSA[43] rescoring. AUTAC binding to Mcl1 was energetically favored (average $\Delta G_bind \approx -90.9$ kcal/mol) relative to Bcl2 (−60.3 kcal/mol) and Bclxl (−53.4 kcal/mol) (Table 1). This preference was driven primarily by more favorable van der Waals

interactions in Mcl1, with additional contributions from electrostatic complementarity, which was markedly reduced in Bclxl. Because productive AUTAC function requires solvent accessibility of the degradation tag, solvent-accessible surface area (SASA) analysis [44] was performed on the FBnG moiety. In the highest-ranked Mcl1 complex, FBnG retained 77% of its free-state SASA, whereas exposure was substantially reduced in Bcl2 (55%) and Bclxl (46%) (Table 1). Thus, despite preserved warhead binding, FBnG becomes progressively more buried in Bcl2- and Bclxl -bound conformations. Together, these results support a model in which selective Mcl1 targeting arises from favorable surface topology at the BH3-groove periphery that permits solvent-exposed presentation of the degradation tag. In contrast, steric confinement in Bcl2 and Bclxl limits FBnG accessibility, providing a structural rationale for preferential Mcl1 targeting despite conserved warhead engagement.

To further verify the selectivity of AUTAC, we evaluated its effect on Bcl2 family proteins in the U266B1 cell line across various concentrations (Fig. 1C). AUTAC reduced Mcl1 protein levels in a dose- and time-dependent manner without an observable impact on both Bclxl and Bcl2. Additionally, AUTAC increased LC3 I/II levels, indicating activation of the autophagic machinery (Fig. 1C). To assess whether AUTAC induces non-selective autophagy through which Mcl1 may be degraded, we compared its effects with starvation-induced autophagy, an approach known to trigger non-selective protein degradation [45-47] (Supplementary Fig. 1D and E). Initially, we validated that autophagy was induced by starvation using LysoTracker staining (Supplementary Fig. 1D). To further confirm autophagy induction, we performed an autophagic flux assay (Supplementary Fig. 1E). Treatment with chloroquine (CQ) in combination with starvation led to greater accumulation of LC3II compared to CQ alone, indicating an active autophagic activity. Under starvation, Mcl1 levels remained largely unchanged (Fig. 1D), suggesting that Mcl1 is not efficiently targeted by non-selective autophagy. Importantly, the individual components of AUTAC (FBng and the Mcl1-binding moiety) did not affect Mcl1 expression when applied separately (Fig. 1D), confirming that the degradation of Mcl1 is dependent on the full AUTAC construct and indicates its selectivity. We further evaluated the selectivity of the AUTAC for Mcl1 degradation by examining several unrelated proteins, including mTOR, p53, HSP70, HSP60, ERK, and ULK1, whose protein levels were not affected by AUTAC treatment (Supplementary Fig. 2A). These results were further supported by immunofluorescence staining of U266B1 cells treated with AUTAC for 24 and 48 hours, which revealed a time-dependent reduction in Mcl1 levels, accompanied by LC3B and LAMP1 accumulation. Notably, increased colocalization between Mcl1 and LAMP1 or LC3B was observed at 24 hours (Supplementary Fig. 2B).

To confirm the autophagy-dependent mechanism of AUTAC, we pharmacologically inhibited the autophagic machinery using CQ [48] and 3-Methyladenine (3-MA) [49]. This inhibition rescued AUTAC-mediated degradation of Mcl1 in U266B1 cells (Fig. 1E). Moreover, combining AUTAC with CQ led to greater LC3II accumulation compared to CQ alone, consistent with enhanced autophagic flux (Fig. 1E). Genetic knockdown of ATG5 similarly alleviated AUTAC-mediated Mcl1 degradation (Fig. 1F). These findings establish that AUTAC selectively targets Mcl1 for degradation through autophagy.

We next examined the functional impact of AUTAC-mediated Mcl1 degradation on cell viability. Treatment with AUTAC reduced the viability of U266B1 and RPMI-8226 cells in a time-dependent manner with an IC□□ of approximately 5μM after 48 h (Fig. 1G). To determine whether this reduction resulted from inhibited proliferation or induction of apoptosis, we performed western blot analysis for cleaved caspase 3 and cleaved PARP. AUTAC treatment led to robust accumulation of both cleaved caspase 3 and cleaved PARP at 24 and 48 hours (Fig. 2H), indicating activation of apoptotic pathways. These findings were corroborated by a trypan blue exclusion assay, which showed that AUTAC induced approximately 50% cell death at 48 hours, increasing to around 60% by 72 hours (Fig. 2I). Collectively, these data demonstrate that AUTAC induces apoptotic cell death in U266B1 cells. To confirm the specificity of this effect, we assessed whether the individual components of AUTAC (FBnG or the Mcl1-binding moiety) were capable of inducing apoptosis on their own. Neither component, when applied separately, nor 24-hour starvation treatment resulted in caspase 3 cleavage (Fig. 2J). These findings indicate that both Mcl1 binding and the autophagy-targeting function are required for AUTAC's activity, highlighting the selectivity and functional integrity of the full AUTAC construct.

To elucidate the mechanism underlying AUTAC-induced autophagy, we first excluded the possibility that Mcl1 AUTAC generally induce autophagy by comparing the Mcl1 AUTAC with an unrelated MetAP2-targeting AUTAC. The MetAP2 AUTAC did not affect Mcl1 levels and failed to induce autophagy, in contrast to the Mcl1 AUTAC (Supplementary Fig. 3A). These findings were further confirmed by autophagic flux inhibition assays (Supplementary Fig. 3B). We next excluded the involvement of the mTOR pathway by comparing the effects of Mcl1 AUTAC with rapamycin. While rapamycin clearly inhibited phosphorylated mTOR (p-mTOR) and the phosphorylation of its downstream target S6 and induced autophagy, Mcl1 AUTAC did not affect the phosphorylation status of these targets (Supplementary Fig. 3C and D). Furthermore, rapamycin did not alter Mcl1 protein levels, whereas AUTAC led to a significant reduction in Mcl1 protein level (Supplementary Fig. 3C). We further showed that the intact AUTAC molecule, but not its individual components—the Mcl1-binding moiety or FBnG—induces autophagy (Supplementary Fig. 3E), confirming that AUTAC-mediated autophagy is a selective process rather than a nonspecific induction of general autophagy. Based on these findings, we hypothesized that AUTAC promotes autophagy via targeted degradation of Mcl1. First, we demonstrated that AUTAC-mediated autophagy is dependent on Mcl1. Knockdown of Mcl1 markedly abrogated AUTAC-induced autophagic activity, as evidenced by diminished LC3II accumulation following co-treatment with AUTAC and CQ in $Mcl1^{KD}$ cells compared with their control counterparts (Supplementary Fig. 3F). Two main molecular mechanisms have been discussed in the scientific literature: (1) Mcl1 is essential for maintaining mitochondrial integrity, and its inhibition leads to increased reactive oxygen species (ROS) [50,51], which in turn induce autophagy [52,53]; and (2) degradation of Mcl1 leads to dissociation from Beclin1, thereby activating Beclin1-dependent autophagy [54,55]. To test the first hypothesis, we treated cells with AUTAC in the presence of N-acetylcysteine (NAC), a known ROS scavenger[56], and assessed autophagic flux. While AUTAC in combination with CQ led to greater accumulation of LC3II compared to CQ alone, NAC treatment did not block this effect (Supplementary Fig. 3G). This suggests that AUTAC-mediated autophagic flux is not dependent on ROS generation. To investigate the second hypothesis, we performed co-immunoprecipitation to assess whether AUTAC affects the interaction between Mcl1 and Beclin1 (Fig. 1K). Interestingly, AUTAC

reduced the binding between Mcl1 and Beclin1 (Fig. 1K) and increased the phosphorylation of Beclin1 (Supplementary Fig. 3H), suggesting that AUTAC liberates Beclin1, leading to its activation and subsequent induction of autophagy.

Collectively, we provide comprehensive evidence demonstrating that AUTAC selectively targets Mcl1, induces cell death in multiple myeloma cell lines, and triggers a specific, Beclin1-dependent autophagy process.

AUTAC selectively degrades Mcl1 through TRAF6/UBC13/p62(SQSTM1) axis

Takahashi et al. [23] demonstrated that AUTAC technology promotes K63-linked polyubiquitination of target proteins. The selective autophagy receptor, p62/SQSTM1, recognizes and binds these K63-linked ubiquitin chains via its UBA (Ubiquitin-Associated) domain [57,58]. Through its LIR (LC3-interacting region) motif, p62 subsequently interacts with LC3 on the autophagosome membrane [59,60], facilitating the selective degradation of ubiquitinated cargo by the autophagic machinery. To investigate whether our AUTAC compound operates through this mechanism, we performed immunofluorescence staining on U266B1 cells treated with AUTAC at 5 and 10 μM for 24 hours. We observed clear colocalization of Mcl1 with K63, p62, and LC3B following AUTAC treatment (Fig. 2A). We further confirmed these results by co-immunoprecipitation, which showed that AUTAC increased the binding of Mcl1 to both K63-linked ubiquitin and p62/SQSTM1 (Fig. 2B). Notably, knockdown of p62/SQSTM1 disrupted the colocalization between LC3B and Mcl1 (Fig. 2C), suggesting that AUTAC mediates K63-linked ubiquitination of Mcl1, which is then recognized and delivered to LC3 by p62 for selective autophagic degradation. To further confirm the p62/SQSTM1-dependent mechanism of action, U266B1^{WT} and U266B1 p62^{KD} cells treated with AUTAC (5 μM) for 24h, where AUTAC-mediated degradation of Mcl1 was abolished upon p62 knockdown compared to its parental counterpart (Fig. 2D). Furthermore, knockdown of p62 abrogated AUTAC-induced accumulation of cleaved caspase 3 and cleaved PARP, indicating that p62 is required for AUTAC-mediated apoptotic signaling (Fig. 2D). These results strongly support the conclusion that AUTAC induces selective autophagic degradation of Mcl1 via the cargo receptor p62/SQSTM1.

Then, we investigated which ligases are involved in AUTAC-mediated Mcl1 degradation. Choi et al. [61] previously demonstrated that Mcl1 undergoes K63-linked ubiquitination mediated by TRAF6. Building on this, we postulated that TRAF6, in concert with the E2 conjugating enzyme UBC13, orchestrates AUTAC-induced K63 ubiquitination of Mcl1. Pharmacological inhibition with either C25-140, a selective TRAF6-UBC13 interaction disruptor [62], or NSC697923, a potent UBC13 inhibitor [63], completely abrogated AUTAC-driven Mcl1 degradation (Supplementary Fig. 4A). Complementary genetic approaches corroborated these findings, as siRNA-mediated depletion of TRAF6 or UBC13 markedly suppressed AUTAC-induced Mcl1 degradation and significantly diminished apoptosis, as evidenced by reduced PARP cleavage (Fig. 2E and F). Together, these results establish TRAF6 and UBC13 as essential mediators of AUTAC-driven K63 ubiquitination and degradation of Mcl1, thereby underscoring the mechanistic selectivity of AUTAC in targeting this anti-apoptotic protein.

To further delineate the mechanism underlying AUTAC-induced cytotoxicity, we assessed whether selective degradation is required for its anti-tumor activity. AUTAC treatment alone reduced U266B1^{WT} cell viability by more than 50%. However, knockdown of p62,

TRAF6, or UBC13 substantially blunted this cytotoxic response (Fig. 2G). These results demonstrate that AUTAC-driven cell death is mechanistically dependent on targeted Mcl1 degradation and strongly support the selectivity and pathway fidelity of the AUTAC system.

Autophagy Induction Augments the AUTAC-Mediated Degradation of Mcl1

We hypothesized that combining an autophagy inducer with AUTAC could enhance its ability to degrade Mcl1. To test this notion, we induced autophagy in U266B1 cells via starvation [64], which was confirmed by lysotracker staining, the autophagic flux inhibition assay and the degradation of p62 (Supplementary Fig. 1D, E and 4B). Treatment of U266B1 cells with 5 μM AUTAC for 24 hours in conjunction with starvation resulted in more pronounced Mcl1 degradation compared to AUTAC alone (Supplementary Fig. 4B).

Carfilzomib (CFZ), a first-line proteasome inhibitor for relapsed and refractory multiple myeloma [65], has been shown by our group and others to induce autophagy [13,18,19,66]. Consistent with these reports, CFZ treatment induced autophagy in U266B1, MM.1S, RPMI-8226 cells, as evidenced by lysotracker staining and the autophagic flux inhibition assay, (Supplementary Fig. 5A, B and C). This induction of autophagic flux was also observed in the proteasome inhibitor-resistant U266B1^{R} cells (Supplementary Fig. 5C). We next evaluated the combined effect of CFZ and AUTAC on Mcl1 levels. CFZ enhanced AUTAC-mediated Mcl1 degradation across multiple myeloma cell lines, including U266B1, MM.1S, RPMI-8226, and AMO-1, with a concurrent increase in autophagic flux, as shown by LC3I/II levels (Fig. 3A). Furthermore, this effect was recapitulated in proteasome inhibitor-resistant multiple myeloma cell lines, such as U266B1^{R} and AMO-1^{R} (Fig. 3B). Notably, LC3II levels differed significantly [67], particularly in MM.1S and RPMI-8226 cells. To determine whether this reflected ongoing autophagic activity, we conducted autophagic flux inhibition assay in the presence of CQ. CQ in combination with CFZ led to a marked increase in LC3II levels in both cell lines as compared to CQ alone (Supplementary Fig. 5B), indicating that LC3II is actively degraded [67]. These results confirm the presence of a highly dynamic and functional autophagic flux.

We then extended this approach to solid tumor non-small cell lung cancer (NSCLC) cell lines NCI-H1975 and proteasome inhibitor-resistant NCI-H1975^{R}. AUTAC alone demonstrated significant efficacy in degrading Mcl1, accompanied by autophagy induction, as indicated by increased LC3I/II levels (Fig. 3C). The combination of CFZ (2.5 or 10 nM) with AUTAC further enhanced Mcl1 degradation and autophagic responses compared to AUTAC alone in both cell lines (Fig. 3C).

To explore whether CFZ could amplify the Mcl1 degradation achieved with lower doses of AUTAC, we treated U266B1 cells with CFZ (10 nM) in combination with varying AUTAC doses (500 nM, 1 μM, and 5 μM). This combination resulted in greater Mcl1 degradation compared to each dose of AUTAC alone, along with increased autophagic flux confirmed by LC3I/II accumulation (Fig. 3D).

Finally, we validated CFZ's ability to enhance Mcl1 degradation by AUTAC using immunofluorescence staining in U266B1 cells treated with AUTAC and/or CFZ for 16 hours. While AUTAC alone reduced Mcl1 levels, the combination with CFZ led to a more pronounced

reduction (Fig. 3E and F). Both AUTAC and CFZ alone increased LC3B and the lysosomal marker LAMP1 levels, indicative of active autophagic flux; however, the combination treatment resulted in significant accumulation of these markers. Increased co-localization of Mcl1 with LC3B and LAMP1 was observed in U266B1 cells treated with AUTAC alone or in combination with CFZ (Fig. 3E and F). Taken together, our findings establish that autophagy inducers, particularly CFZ, enhance the ability of AUTAC to degrade Mcl1 via amplifying autophagic flux.

CFZ-mediated Enhancement of AUTAC Activity is Dependent on NRF1, p62/SQSTM1 and Functional Autophagy.

We have previously demonstrated that NRF1 is a key regulator of cellular responses to proteotoxic stress induced by proteasome inhibition [68-71]. NRF1 facilitates the upregulation of proteasome genes to restore proteasome activity and promotes autophagy, providing cells with alternative pathways to degrade ubiquitylated protein aggregates. These mechanisms enable cells to mitigate proteotoxic stress. Notably, our group has shown that NRF1 knockout abolishes carfilzomib-induced autophagy, resulting in the accumulation of autophagosome vacuoles in NRF1-deficient cells [13]. Initially, we showed that AUTAC-mediated activities—including Mcl1 degradation (Fig. 4A), autophagy induction, and cell death, as evidenced by cleaved caspase 3, PARP cleavage, and reduced cell viability (Fig. 4A and B)—are not dependent on NRF1. To further validate our previous findings, we examined the effects of NRF1 knockout on CFZ–mediated transcriptional responses. NRF1 knockout abolished CFZ-induced upregulation of autophagy-related genes, including p62/SQSTM1, ATG4A, CTSD, GABARAPL1, and VPS37A, as well as proteasome-related genes, including PSMA7, PSMC4, and PSMD12 (Fig. 4C). Consistently, NRF1 knockout also suppressed CFZ-induced upregulation of autophagy-related proteins, including p62/SQSTM1, CTSD, GABARAPL1, and LAMP1 (Fig. 4D). Furthermore, NRF1 knockout abolished CFZ-mediated autophagy induction, as confirmed by autophagic flux inhibition assay using CQ (Fig. 4E).

We then assessed the impact of NRF1 knockout on Mcl1 degradation mediated by the combination of AUTAC and CFZ in U266B1 cells. NRF1 knockout rescued Mcl1 levels, preventing the reduction achieved by the combination of AUTAC and CFZ in wild-type cells. This effect was accompanied by diminished autophagic flux, as evidenced by decreased LC3I/II levels in NRF1-deficient cells compared to wild-type controls (Fig. 4F). To further validate the role of autophagy in this context, we employed an orthogonal approach. Knockdown of ATG5, an essential autophagy gene, significantly attenuated the Mcl1 degradation observed with the CFZ and AUTAC combination in U266B1 cells (Fig. 4G). Together, these findings underscore the pivotal role of NRF1 in CFZ-induced autophagy and highlight the necessity of functional autophagy for the synergistic activity of CFZ and AUTAC in degrading Mcl1.

We further validated the role of p62/SQSTM1 in mediating AUTAC-induced Mcl1 degradation, even in combination with CFZ. The knockdown of p62 completely abolished Mcl1 degradation induced by the combination of CFZ and AUTAC (Fig. 4H), underscoring the essential role of p62 in mediating this selective degradation pathway.

Combination of AUTAC and Carfilzomib Overcomes Proteasome Inhibitor Resistance *In Vitro* and Suppresses Tumor Growth *In Vivo*

Chemotherapeutic agents modulate autophagy in distinct ways, including cytotoxic, cytostatic, non-protective, and cytoprotective forms [72-74]. CFZ has been shown to induce cytoprotective autophagy [18-20,66], which we confirmed in our study using autophagy inhibitors like CQ and bafilomycin (BAF), which enhanced CFZ toxicity (weak synergy except in U266B1 cells with CQ) in both U266B1 cells and proteasome inhibitor-resistant U266B1^{R} cells (Supplementary Fig. 5C, D, and E). Furthermore, to substantiate the role of Mcl1 in mediating resistance to proteasome inhibitors, we generated Mcl1-overexpressing U266B1 cells (U266B1 Mcl1^{OE}) and assessed their viability in response to varying concentrations of CFZ, in comparison to U266B1^{WT} and the resistant U266B1^{R} cell line (Supplementary Fig. 6A and B). U266B1 Mcl1^{OE} cells demonstrated a marked resistance to CFZ relative to their wild-type counterparts (Supplementary Fig. 6A). Additionally, western blot analysis revealed elevated Mcl1 expression levels in U266B1^{R} cells compared to parental U266B1 (Supplementary Fig. 6B), further corroborating the pivotal role of Mcl1 in conferring resistance to proteasome inhibition in multiple myeloma.

Given AUTAC's ability to degrade Mcl1 in an autophagy-dependent manner, we hypothesized that combining AUTAC with CFZ could enhance its cytotoxic effects. Indeed, this combination reduced the viability of multiple myeloma cell lines, including U266B1, AMO-1, MM.1S, and RPMI-8226, while also sensitizing resistant lines (U266B1^{R} and AMO-1^{R}) to CFZ (Fig. 5A). This reduction in cell viability occurred in a strongly synergistic manner across all tested cell lines, as confirmed by Bliss synergy scoring. Western blot analysis revealed increased cleaved caspase 3 levels, indicating apoptosis induction in both wild-type and resistant cells (Fig. 5B). We further demonstrated that AUTAC significantly potentiated CFZ-mediated cytotoxicity in U266B1 Mcl1^{OE} (Supplementary Fig. C). This effect was accompanied by a pronounced reduction in Mcl1 protein level and a marked increase in apoptotic markers, including cleaved caspase 3 and cleaved PARP (Supplementary Fig. D). To further validate the selectivity of AUTAC- and CFZ-induced cytotoxicity and to determine its dependence on p62/SQSTM1, we compared U266B1^{WT} cells with U266B1 p62^{KD} cells (Fig. 5C). Notably, AUTAC enhanced CFZ sensitivity in U266B1^{WT} cells, whereas this effect was completely abrogated in p62^{KD} cells (Fig. 5C). Collectively, these findings underscore the selective capacity of AUTAC to redirect cytoprotective autophagy toward targeted Mcl1 degradation in a p62-dependent manner, thereby amplifying apoptotic cell death.

To confirm the therapeutic superiority of the combination, we investigated its effect *in vivo* using NSG mice subcutaneously injected with U266B1 cells. Treatment with CFZ alone resulted in a significant reduction in tumor volume (Fig. 6A); however, subsequent treatment with AUTAC led to a further reduction in tumor volume compared with either treatment alone (Fig. 6A), without significant toxicity (Fig. 6B). Mechanistically, CFZ enhanced the ability of AUTAC to reduce Mcl1 protein levels, while the combination had no impact on Bclxl or Bcl2 levels (Fig. 6C). Furthermore, autophagy induction was evidenced by reduced p62/SQSTM1 levels and increased LC3II accumulation (Fig. 6B). Subsequently, we conducted a comparative analysis of AUTAC against several well-characterized Mcl1 inhibitors, including S63845, AMG 176, UMI-77, AZD-5991, and A-1210477. Given the well-documented cardiotoxicity observed with Mcl1 inhibition in clinical settings, we specifically assessed the cytotoxic profiles of these

compounds in AC16 human cardiomyocytes. Although AUTAC (IC_{50} = 5 μM) was less potent against U266B1 cells compared to AMG176 (IC_{50} = 750 nM), S63845 (IC_{50} = 200 nM), and AZD-5991 (IC_{50} = 100 nM), it demonstrated a more favorable safety profile. Notably, AUTAC exhibited no detectable cardiotoxicity in this model. In contrast, S63845 (AC16 IC_{50} = 100 nM), AMG176 (AC16 IC_{50} = 2.5 μM), and AZD-5991 (AC16 IC_{50} = 100 nM) induced pronounced cytotoxic effects (Fig. 5D). These findings highlight the potentially superior cardiac safety profile of AUTAC. Next, we evaluated the synergistic potential of these Mcl1 inhibitors in combination with CFZ in both U266B1 and its resistant counterpart, U266B1R (Fig. 7). Although AUTAC, along with UMI-77 and A-1210477, demonstrated comparatively lower standalone potency relative to S63845, AMG 176, and AZD-5991, AUTAC exhibited the highest degree of synergy with CFZ across both cell lines, as quantified by Bliss synergy scores (Fig. 7). In contrast, the other inhibitors displayed variable interactions ranging from weak synergy, as observed with A-1210477, to merely additive effects or even antagonism with to S63845, UMI-77, AMG 176, and AZD-5991 (Fig. 7), in consistent with several reports [75-78]. These findings underscore the unique advantage of AUTAC in harnessing CFZ-induced autophagic flux to enhance Mcl1 degradation, thereby potentiating its combinatorial efficacy.

In solid tumors, including non-small cell lung cancer (NSCLC), proteasome inhibitors (PIs) have shown limited efficacy [6-8]. To improve PI efficacy in this context, we evaluated the combination of AUTAC and CFZ in wild-type (NCI-H1975) and bortezomib-resistant (NCI-$H1975^R$) NSCLC cells. The combination significantly reduced cell viability compared to either treatment alone (Fig. 8A) and increased cleaved caspase 3 accumulation, confirming apoptosis (Fig. 8B). This reduction in cell viability occurred in a strongly synergistic manner in both cell lines, as confirmed by Bliss synergy scoring (Fig. 8A). Colony formation assays demonstrated that while AUTAC or CFZ alone moderately reduced the colony-forming ability of NCI-H1975 cells, their combination had a significantly stronger effect. In NCI-$H1975^R$ cells, which showed minimal response to CFZ alone, the combination markedly inhibited colony formation (Fig. 8C). These findings highlight the potential of AUTAC to enhance PI efficacy by disrupting cytoprotective autophagy and promoting apoptotic cell death in both hematologic and solid tumors.

DISCUSSION

Proteasome inhibitors (PIs) have transformed the treatment landscape for multiple myeloma, eliciting robust initial responses and significantly improving patient outcomes and survival rates. However, disease relapse and acquired resistance remain major clinical challenges [79]. Several adaptive mechanisms could underlie resistance to PIs, including NRF1-driven autophagy and the antiapoptotic role of Mcl1 [13-15,26-28]. In this study, we demonstrated that leveraging Mcl1-targeting AUTAC enhances the efficacy of CFZ in both hematologic malignancies, both *in vitro* and *in vivo*, and solid tumors, including proteasome inhibitor-resistant models.

The concept of AUTAC originates from studies on selective autophagy triggered by infection, where nitric oxide (NO) and ROS mediate the degradation of bacterial proteins. Specifically, NO facilitates the conversion of cytoplasmic cyclic guanosine monophosphate

(cGMP) to 8-nitro-cGMP, which modifies bacterial surface proteins via S-guanylation, targeting them for autophagic degradation [22,34,80-82]. Takahashi et al. [23] harnessed this pathway to develop the first and second generations of AUTACs, substituting cysteine with a pyrazole ring in the degradation tag. Building on this framework, we developed a second-generation AUTAC to selectively degrade Mcl1. Our results demonstrate that AUTAC selectively targets Mcl1 for degradation among members of the Bcl2 protein family. Given that AUTAC induces the autophagic machinery, we confirmed that this effect is not attributable to nonspecific autophagic flux. Moreover, our data demonstrates that AUTAC activates autophagy in a Beclin1-dependent manner, rather than through mTOR suppression, nonspecific global autophagy induction, or indiscriminate ROS generation. These findings are consistent with previous reports showing that several Mcl1 inhibitors disrupt the interaction between Mcl1 and Beclin1, thereby promoting Beclin1-mediated autophagy [54,55,83,84]. Critically, we show that the intact AUTAC molecule is required for selective Mcl1 degradation and autophagy induction, as neither the Mcl1-binding ligand nor the FBng tag alone was sufficient to elicit these effects. We further confirmed the autophagy-dependent mechanism of Mcl1 degradation by AUTAC, validated pharmacologically using early and late autophagy inhibitors (3-MA and CQ, respectively) and genetically via ATG5 knockdown.

The AUTAC technology offers distinct advantages over ubiquitin-proteasome system (UPS)-based degradation strategies [23,85]. Unlike UPS-targeting approaches, which are limited to soluble proteins, AUTAC has the potential to target a broader range of cellular cargoes, including non-proteinaceous biomolecules and organelles such as mitochondria [23,85]. In terms of kinetics, we observed initial signs of AUTAC-mediated protein degradation as early as 3 hours post-treatment (data not shown), with degradation efficiency increasing over time. This gradual onset is likely reflective of the more complex, multistep nature of autophagy compared to the relatively direct mechanism of UPS-mediated degradation [23,85]. Mechanistically, AUTAC exerts its degradative function through K63-linked polyubiquitination of target proteins, as first demonstrated by Takahashi et al.[23]. In their study, the degradation activity of AUTAC was abrogated upon genetic elimination of p62/SQSTM1, highlighting the essential role of this selective autophagy receptor in the pathway. In line with these findings, our data confirm that AUTAC promotes the colocalization of Mcl1 with K63-linked ubiquitin chains, p62/SQSTM1, and the autophagosomal marker LC3B, suggesting that Mcl1 is recruited into autophagosomes via the canonical selective autophagy machinery. We further corroborated the colocalization findings by Co-IP analysis, which demonstrated that AUTAC treatment enhanced the association of K63-linked ubiquitin and p62/SQSTM1 with Mcl1. Furthermore, shRNA-mediated depletion of p62 abolished the AUTAC-induced degradation of Mcl1, further substantiating the requirement of this receptor in mediating cargo selectivity. The role of p62/SQSTM1 is particularly significant, as it serves as a molecular bridge linking ubiquitinated substrates to the autophagosome [57-60]. It binds K63-polyubiquitinated proteins via its C-terminal ubiquitin-associated (UBA) domain and facilitates their sequestration into autophagosomes through direct interaction with LC3 via its LC3-interacting region (LIR) [57-60]. This mechanism reinforces the specificity of AUTAC in targeting distinct proteins, such as Mcl1, for autophagic degradation.

Interestingly, 8-nitro-cGMP has been reported to act as a molecular tag that facilitates K63-linked polyubiquitination [22] . In this context, Yamada et al.[86] demonstrated that the FBXO2-SCF E3 ubiquitin ligase complex recognizes bacterial surface glycans modified with 8-nitro-cGMP, thereby inducing K63-linked polyubiquitination and initiating xenophagic clearance. Therefore, we investigated the specific E3 and E2 ligases responsible for mediating AUTAC-induced K63-linked ubiquitination of Mcl1. Senichkin et al.[87] reported that the E3 ubiquitin ligase TRAF6 mediates K63-linked ubiquitination of Mcl1, resulting in its stabilization rather than proteasomal degradation, which also reported by Sancho et al. [88]. In contrast, proteasomal turnover of Mcl1 is primarily driven by K48-linked ubiquitination, largely mediated by the E3 ligase Mule (also known as HUWE1)[87,89]. Similarly, Choi et al. [61] demonstrated that the viral protein HTLV-1 Tax promotes non-degradative K63-linked ubiquitination of Mcl1, thereby enhancing its stability. These reports confirm that Mcl1 is subjected to K63 ubiquitination, which mediate Mcl1 stabilization and involved in several signaling purposes[88,90-92]. However, under stress conditions, K63-linked ubiquitination can function as an autophagic signal, by promoting recognition by selective autophagy receptors [92-94]. In parallel, our findings demonstrate that AUTAC engages TRAF6 together with UBC13, the principal E2 ubiquitin-conjugating enzyme responsible for K63 chain assembly [95-97], to promote K63-linked ubiquitination of Mcl1. These results reveal a model in which AUTAC selectively harnesses the TRAF6–UBC13 axis to redirect Mcl1 toward degradation, through K63 ubiquitination and subsequent recognition by p62/SQSTM1, thereby reinforcing the mechanistic specificity underlying AUTAC-mediated targeting. Additionally, AUTAC markedly reduced the viability of multiple myeloma and NSCLC cells through robust induction of apoptosis. In contrast, genetic silencing of p62, TRAF6, or UBC13 effectively abolished AUTAC-mediated cytotoxicity, demonstrating that its anti-tumor activity is strictly dependent on the autophagic ubiquitin-tagging pathway and excluding the possibility of off-target effects.

We further exploited the cytoprotective autophagy induced by CFZ, repurposing it as a degradation mechanism for Mcl1. The combination of CFZ and AUTAC markedly reduced Mcl1 levels in both wild-type and proteasome inhibitor-resistant multiple myeloma and NSCLC cells, accompanied by a robust upregulation of autophagic flux. Importantly, NRF1, p62/SQSTM1 and functional autophagy were essential for Mcl1 degradation, as shown through genetic inhibition approaches. These mechanistic insights translated into significant reductions in cellular viability and increased apoptosis, highlighting the ability of AUTAC to sensitize resistant cells to CFZ. We further demonstrated that the combination of AUTAC and CFZ significantly suppressed U266B1 tumor xenografts growth compared with either monotherapy alone. These findings provide a proof of concept that combining proteasome inhibitors can potentiate the degradative capacity of AUTAC technology, suggesting its broader applicability to targets beyond Mcl1. The interplay between autophagy and PI resistance is well-established [18-20,66], and we confirmed that autophagy inhibition using CQ or BAF augmented CFZ-induced cytotoxicity. However, the lack of selective autophagy inhibitors and the adverse effects of existing agents, such as CQ and HCQ, limit their clinical utility [98-101]. This study introduces a novel strategy of harnessing PIs' cytoprotective autophagy, rather than inhibiting it, by targeting resistance-associated proteins like Mcl1 for autophagic degradation.

We also evaluated the efficacy and safety profile of AUTAC in comparison with several classical Mcl1 inhibitors. Among all agents tested, AUTAC exhibited the lowest cytotoxicity toward cardiomyocytes while demonstrating the most pronounced synergistic effect with CFZ. Given the well-documented cardiotoxicity associated with proteasome inhibitor therapy, our findings suggest that AUTAC may serve as a valuable adjunct to enhance the antitumor efficacy of proteasome inhibitors while minimizing their dose-limiting toxicities. This combinatorial approach holds promise for reducing the required dosage of proteasome inhibitors, thereby preserving therapeutic benefit while minimizing off-target adverse effects, particularly in cardiac tissue. Further research is necessary for the structural optimization of AUTAC to enhance its potency and therapeutic efficacy.

MATERIALS AND METHODS

Cell Culture. MM.1S (CRL-2974; ATCC), RPMI-8226 (CCL-155; ATCC), AMO-1, AMO-1 resistant/ AMO-1^{R} (both sensitive and resistant cell lines were obtained from Dr. Bianchi Lab, Division of Hematology, Brigham and Women's Hospital, Harvard Medical School), NCI-H1975 [102], NCI-H1975 resistant/ NCI-$H1975^{R}$ (NCI-H1975 were continuously exposed to increasing concentrations of bortezomib (up to 10 nM) over a period of 10 weeks, with surviving cells maintained in 10 nM), U266B1 resistant/ $U266B1^{R}$ [103], U266B1 (TIB-196; ATCC), U266B1 $ATG5^{KD}$ [104], U266B1 $p62^{KD}$ [104], and their derivatives were grown in Roswell Park Memorial Institute Medium (RPMI) (Gibco), while AC16 cells (CRL-3568; ATCC) were grown in Dulbecco's Modified Eagle Medium (DMEM; Gibco). Both media were supplemented with 10% fetal bovine serum (FBS; Atlanta Biologicals), 1X penicillin-streptomycin (Pen/Strep; Invitrogen) and 5 µg/ml Plasmocin Prophylactic (PP; InvivoGen). All cell lines were grown at 37°C in a humidified incubator with 5% CO2.

Cell line provenance and quality control. Cell lines obtained from ATCC were used according to supplier documentation. Cell lines obtained from external laboratories were used as received. Cell lines were authenticated by the supplier. Mycoplasma contamination was monitored routinely using InvivoGen’s MycoStrip® detection assay and prevented by Plasmocin prophylaxis.

Study Design, Replicates, and Sample Size. Unless otherwise indicated, all *in vitro* experiments were performed with at least three independent biological replicates. Within each independent experiment, assays were performed in technical triplicate, except for cell viability assays, which were performed with six technical replicates per condition.

Sample size justification. Sample sizes for *in vitro* experiments were selected based on prior experience with these assays and expected effect sizes from preliminary work. No formal a priori power calculations were performed for *in vitro* studies.

For animal studies, n values are stated explicitly (see Mouse xenograft model). Group sizes were selected based on prior xenograft experience and expected effect sizes; no formal power calculation was performed.

Inclusion/Exclusion Criteria and Data Exclusion. No animals or biological replicates were excluded from analysis. For *in vitro* studies, experiments were repeated only in the case of clear

technical failure, and these repeats were not based on outcome. Criteria were applied consistently and were not modified post hoc.

Randomization and Blinding. Randomization (animal studies). Xenograft implantation, dosing, and tumor measurements were performed by the Massey Cancer Center Mouse Core. Once tumors reached 75–100 mm^3, mice were randomized into treatment groups using a randomization procedure implemented by the core facility. Baseline tumor volumes did not differ significantly between groups prior to treatment initiation (TV, $P = 0.990$), confirming balanced allocation. Randomization was performed prior to initiation of drug treatment. **Randomization (*in vitro*).** For plate-based assays, wells were assigned to conditions without systematic bias.

Blinding. Investigators were not routinely blinded to treatment allocation during *in vitro* experiments. Xenograft dosing and tumor measurements were conducted by the Massey Cancer Center Mouse Core. Blinding during tumor measurement was performed according to standard core operating procedures when feasible. The study investigators did not participate in tumor measurements. Quantitative analyses (western blot densitometry, fluorescence intensity measurements, and colocalization analyses) were conducted using predefined ImageJ analysis parameters applied uniformly across all conditions to minimize subjective bias.

Western blotting. Cells were plated and treated in six-well plates, then collected at the indicated time points and washed once with ice-cold PBS. Cells lysed using RIPA Buffer (20 mM Tris-HCl pH 7.4, 1% sodium deoxycholate, 1% Triton X-100, 0.1% SDS, 150 mM NaCl, and 1 mM EDTA) containing protease and phosphatase Inhibitor cocktail (Cat No: PI78447; Thermo Fisher Scientific), then incubated on ice for 15 min, and centrifuged at 14,000 rpm for 10 min at 4°C. Protein concentrations were measured by the bicinchoninic acid (BCA) assay. Western blot samples were prepared with 4X Laemmli protein sample buffer (Cat No:1610747; Bio-Rad) with the addition of 2-mercaptoethanol on the day of lysis, followed by boiling for 7 min. 10-15 µg of protein was used for SDS-PAGE, gels were transferred onto Immobilon FL PVDF membranes (Cat No: IPVH00010; Millipore Sigma). Membranes were blocked with 5% blotting grade blocker (Cat No: 1706404; BIO-RAD) in TBST for 1-2 h.

Blots were incubated with the indicated primary antibodies overnight, then washed with TBST and incubated with secondary antibodies for 1 h at room temperature. The antibodies used were LC3B (Cat No:2775S; Cell Signaling) at 1:1,000, NRF1 (Cat No:8052S; Cell Signaling) at 1:1,000, cleaved caspase-3 (Cat No:9661L; Cell Signaling) at 1:500, cleaved PARP (Cat No: 5625S; Cell Signaling) at 1:1000, ATG5 (Cat No: 12994S; Cell Signaling) at 1:1000, SQSTM1/p62 (Cat No:5114S; Cell Signaling) at 1:1000, Mcl1 (Cat No: 5453S; Cell Signaling) at 1:500, Bcl2 (Cat No: 3498S; Cell Signaling) at 1:1,000, Bclxl (Cat No: 2764 S; Cell Signaling) at 1:1,000, TRAF6 (Cat No: 8028S; Cell Signaling) at 1:1,000, UBC13 (Cat No: 4919S; Cell Signaling) at 1:1,000, Beclin1 (Cat No: 3495S; Cell Signaling) at 1:1,000, p-Beclin1 (Ser15) 1:500 (Cat No: D4B7R; Cell Signaling), K63 1:1000 (Cat No: HWA4C4; Invitrogen) and GAPDH (Cat No: 5174S; Cell Signaling) at 1:10,000. Goat anti-Rabbit Igg HRP conjugate antibody (Cat No:1706515; BIO-RAD) at 1:10,000 dilutions. Blots then washed with TBST, then incubated with clarity western ECL substrate (Cat No: 1705060; BIO-RAD, or Cat No: 1705062; BIO-RAD) for 5 minutes. Imaging of the blots was done by the LiCOR Odyssey Fc Imaging System. In all pharmacologic and genetic manipulation experiments, appropriate matched controls were included. DMSO served as the vehicle control for compound treatments.

GFP-expressing control cells (shGFP or KO-GFP) were used as negative controls for knockdown and knockout studies, respectively.

Western blot densitometric analysis was performed using ImageJ software. Band intensities were quantified from at least three independent experiments. Protein expression levels were normalized to the corresponding GAPDH loading control and subsequently expressed relative to the control group.

Co-immunoprecipitation (Co-IP). U266B1 cells were seeded in 6-well plates and treated with AUTAC (10 μM) for 16 h (for K63-linked ubiquitin and p62) or 24 h (for Beclin1). Cells were harvested by centrifugation and lysed in immunoprecipitation (IP) buffer (50 mM Tris-HCl, pH 7.4, 100 mM NaCl, 1 mM EDTA, 1% Triton X-100) supplemented with protease and phosphatase inhibitor cocktails (Thermo Fisher Scientific, Pierce). Lysates were incubated on ice for 10–15 min and clarified by centrifugation at 14,000 rpm for 10 min at 4°C. Protein concentration was determined using a BCA assay. All samples were normalized to equal protein concentrations and adjusted to a final volume of 300 µL with IP buffer. An aliquot of 25 µL was retained as input (total cell lysate). The remaining supernatants were subjected to immunoprecipitation using Protein A/G agarose beads and incubated with anti-Mcl1 antibody (1:50; D2W9E, Cell Signaling Technology). Beads were pre-blocked with 5% BSA for 1 h prior to incubation with lysates. After immunoprecipitation, beads were washed three times with IP buffer and proteins were eluted in Laemmli sample buffer. Eluted proteins and input samples were resolved by SDS–PAGE and analyzed by western blotting as described previously. DMSO served as the vehicle control for compound treatments.

Quantitative real-time PCR (qRT–PCR). U266B1^{WT} and U266B1 NRF1^{KO} cells were seeded in 6-well plates and treated with CFZ (20 nM) for 20 h. Following treatment, cells were washed once with phosphate-buffered saline (PBS) and harvested by gentle scraping in 1 mL PBS. Total RNA was isolated using the RNeasy Mini Kit (Qiagen) with on-column DNase I digestion to remove genomic DNA contamination. Complementary DNA (cDNA) was synthesized from 1 µg of total RNA using iScript Reverse Transcription Supermix (Bio-Rad) according to the manufacturer's instructions. Quantitative real-time PCR was performed using iTaq Universal SYBR Green Supermix (Bio-Rad) on a C1000 Touch Thermal Cycler (Bio-Rad). Transcript levels were normalized to 18S rRNA as the internal reference gene. Relative gene expression was calculated using the ΔΔCt method and analyzed using CFX Manager software (v3.1; Bio-Rad). In all pharmacologic and genetic manipulation experiments, appropriate matched controls were included. DMSO served as the vehicle control for compound treatments. GFP-expressing control cells (KO-GFP) were used as negative controls for knockout studies.

Genes (Human)	Forward Primer (5′–3′)	Reverse Primer (5′–3′)
p62 (SQSTM1)	GGTGAACCTCCAGTCCCTACA	TCATCAGAGAAGCCCATGGA
GABARAPL1	TCGGAAAAGGAAGGAGAAA	TGGCCAACAGGTACTGCAGA
ATG4A	AACCTGGATCCTTCAGTTGC	CAAATCCTCCAGTTGCTCA
CTSD	GGTGAACCTCCAGTCCCTACA	TCATCAGAGAAGCCCATGGA
VPS37A	TGCTTCCTCCACAGTTTCCT	GGATTCTTCCAAACTCATCCA
PSMA7	GGTCCAGTCCTGGAGAAGA	GCTCACATCCATCAGTCTGA
PSMC4	GGAAGACCATGTTGGCAGAG	AAGATGATGGCAGTGGCATT

PSMD12	GTGCGCGACTGACTAACACA	TAGGCAGGAGCTCATTTGCT

Mouse xenograft model. All animal studies were approved by the Virginia Commonwealth University (VCU) Institutional Animal Care and Use Committee (IACUC) (Protocol AD10001417) and conducted in accordance with institutional guidelines and regulations. Animal experiments are reported in compliance with the ARRIVE 2.0 guidelines. Male and female NOD-SCID-IL2Rγ (NSG) mice (4–6 weeks old) were inoculated subcutaneously (unilaterally, right flank) with U266B1 (8×10^6 cells; n =4 mice per treatment group) resuspended in Matrigel in a total volume of 100 µL. Tumor growth was monitored biweekly by manual caliper measurements, and tumor volumes were calculated using the modified ellipsoid formula [105]: $V = (L \times W^2)/2$, where L is the longest diameter and W is the perpendicular diameter. Once tumors reached approximately 75–100 mm^3, mice were randomized into treatment groups and tumor volumes were measured daily. Carfilzomib (5 mg/kg) or an equal volume of vehicle (Captisol) was administered via tail vein injection on days 1, 4, and 7. This was followed by once-daily intraperitoneal injections of vehicle (10% DMSO, 40% PEG300, 5% Tween-80, and 45% saline) or AUTAC (50 mg/kg). Tumors were harvested at the study endpoint (tumor volume of ~1500 mm^3) for downstream analyses. No animals were excluded.

Cell viability. The CellTiter-Glo assay was utilized as the screening protocol for drugs action. Cells were plated in 96 well plate at a density of 2500-6000 cells per well and then were treated with the indicated conditions. The CellTiter-Glo assay (G7570; Promega) was performed according to standard protocol and luminescence was quantified using a POLARStar Optima cell microplate reader. Unless otherwise indicated, technical replicates: 6 wells per condition per experiment. Biological replicates: ≥3 independent experiments. The figures were generated using GraphPad Prism software. Bliss score and synergy figures were generated using synergy finder [+] [106]. DMSO served as the vehicle control for compound treatments. GFP-expressing control cells (shGFP) were used as negative controls for knockdown.

Cell death. The percentage of dead cells were calculated using trypan blue exclusion assay [107]. U266B1 cells were treated with AUTAC 5 µM for 48 and 72h. Cells were stained with trypan blue, then counted. Experiments were repeated independently ≥3 times. The figures were generated using GraphPad Prism software. DMSO served as the vehicle control for compound treatments.

Clonogenic assay. Cells plated in 6 well-plates at density of 2500-3000 cells per well, then allowed to adhere overnight. Cells treated with AUTAC 5 µM and/or CFZ (2.5-10 nM) for 72h, then drug removed, and cells replenished with fresh media every 3 days for total of 9 days. Plates were fixed with methanol, stained with crystal violet, and manually counted. Experiments were repeated independently ≥3 times. The figures were generated using GraphPad Prism software. DMSO served as the vehicle control for compound treatments.

Lysotracker imaging. Cells were plated in 6 well plates and starved (treated with FBS depleted media) or treated with CFZ 10nM for 24h. Cells stained with DAPI (Cat No: PI62249; ThermoFisher) and Lysotracker (Cat No: L7528; ThermoFisher) stains according to the manufacture protocol. Fluorescence images of cells were taken using a brightfield inverted microscope (20X objective, Q-Color3™ Olympus Camera; Olympus, Tokyo, Japan). The merged images and quantification were generated using Image J software. The figures were

generated using GraphPad Prism software. DMSO served as the vehicle control for compound treatments.

U266B1 NRF1^{KO} cells. Edit-R human NRF1 all-in-one lentivirus sgRNA (Catalog#: SGSH12178-249373759) and Edit-R all-in-one lentiviral sgRNA hEF1a-EGFP non-targeting control (Catalog#: GSGC12062) were purchased from Horizon. For generating lentiviral supernatant, HEX 293 LXT cells were grown to 80% confluency in a 10 cm dish and transfected with lipofectamine (L3000015, ThermoFisher Scientific) with 8 µg lentivirus construct, 6 µg psPAX2 (packaging plasmid, 12260, Addgene), 4 µg pmD2.G (envelope plasmid, 12259, Addgene). Cells were incubated in OptiMEM (31985070, Thermo Fisher Scientific) transfection reagent overnight at 37 °C. The OptiMEM was replaced with fresh 5 mL 5% FBS full media, and cells were incubated at 10% CO_2. 48 hours post-transfection, the supernatant containing virus was harvested and immediately filtered to remove cell debris. U266B1 cells were transduced with lentiviral supernatant supplemented with fresh growth media and 8 µg/mL polybrene. Successfully transduced cells were then selected by fluorescence-activated cell sorting (FACS). To confirm NRF1 knockout in U266B1 cells, WB was performed. U266B1 and U266B1 NRF1^{KO} cells were treated with 10 nM CFZ for 6 hours.

TRAF6,UBC13, and Mcl1 Knockdown. Knockdown was achieved using smart pool (Dharmacon) of small interfering RNAs (siRNAs). For TRAF6, GGAGAAACCUGUUGUGAUU, GGACAAAGUUGCUGAAAUC, GUUCAUAGUUUGAGCGUUA, and GAUAUGAUGUAGAGUUUGA. For UBC13, GCACAGUUCUGCUAUCGAU, GAGCAUGGACUAGGCUAUA, CAGAUGAUCCAUUAGCAAA, and GCGGAGCAGUGGAAGACCA. For Mcl1, CGAAGGAAGUAUCGAAUUU, AGAACGAAUUGAUGUGUAA, GGACCAACUACAAAUUAAU, GCUACGUAGUUCGGGCAAA. . Cells were transfected with gene-specific siRNAs using the Lonza 4D-Nucleofector X Unit and SF Cell Line 4D-Nucleofector X Kit L (Catalog #: V4XC-2012) according to the manufacturer's instructions. Knockdown efficiency was verified by immunoblotting 72 h post-transfection. GFP-expressing control cells (shGFP) were used as negative controls for knockdown.

Immunofluorescence. For immunofluorescence (IF), U266B1^{WT} or U266B1 p62^{KD} cells were treated with 5 or 10 µM AUTAC for either 24 or 48 hours, or with 10 nM CFZ, 5 µM AUTAC, or a combination of AUTAC and CFZ for 16 hours. The treated cells were seeded onto 12-mm-diameter glass coverslips placed in 12-well culture dishes pre-coated with 0.01% poly-L-lysine (Sigma-Aldrich, P4832) for 1 hour. Cells were washed with PBS before fixation in 4% paraformaldehyde for 30 minutes at room temperature (RT). Following fixation, cells were rinsed with PBS and blocked for 1 hour in a blocking buffer containing 5% BSA and 0.1% Triton X-100 in PBS. The cells were then incubated overnight at 4°C with the designated primary antibodies including LAMP1 (Cat. No. 15665S, Cell Signaling Technology), LC3B (Cat. No. 83506S, Cell Signaling Technology), K63 (Cat. No. 14-6077-82 Thermo Fisher), p62/SQSTM1 (Cat. No. 88588 Cell Signaling Technology), and Mcl1 (Cat. No. 94296S, Cell Signaling Technology). After three washes with PBS, the cells were incubated with the corresponding secondary antibodies (Alexa Fluor 488 anti-mouse; Lot: 160324, Jackson ImmunoResearch, Alexa Fluor 555 goat anti-mouse IgG; Lot: WA316324, Invitrogen, and Alexa Fluor 594 goat anti-rabbit IgG; Lot: 1608397, Life Technologies). The secondary antibodies were diluted in antibody solution (5% BSA and 0.1% Triton X-100 in PBS) and incubated for 2 hours at room temperature (RT). Nuclear staining was performed by incubating the cells with

4',6-diamidino-2-phenylindole (DAPI; Lot: WE3286201, Thermo Scientific) for 3 minutes at RT in the dark. Cells were washed three times with PBS, mounted onto glass slides using a mounting medium (Vectashield), and imaged using a Zeiss Laser Scanning Microsope (LSM) 700 fitted with a 63x oil-immersion lens. Images were analyzed, processed and quantified using ImageJ software. Colocalization was assessed using JACoP with Pearson's correlation coefficient and Manders' coefficients (M1, M2). Background subtraction and thresholding were applied consistently across images. The figures were generated using GraphPad Prism software. In all pharmacologic and genetic manipulation experiments, appropriate matched controls were included. DMSO served as the vehicle control for compound treatments. GFP-expressing control cells (sh-GFP) were used as negative controls for knockdown.

Molecular docking studies. *Protein preparation.*[108] Crystal structures of human MCL1 (PDB ID: 6YBL), BCL2 (PDB ID: 2XA0), and BCL-XL (PDB ID: 1R2D) were obtained from the Protein Data Bank. Bond orders were assigned, missing hydrogens were added, and protonation states were optimized using Epik at physiological pH (7.0 ± 0.5).[109] Hydrogen-bonding networks were refined, and crystallographic water molecules were removed except where structurally conserved or involved in key interactions. The prepared protein structures were subjected to restrained energy minimization using the OPLS4 force field[110], converging heavy atoms to an RMSD of 0.3 Å.

Ligand preparation. The AUTAC molecule and the corresponding warhead fragment were prepared using LigPrep with the OPLS4 force field. Ionization states and tautomers were generated using Epik at physiological pH, and all salts were removed. Warhead-only reference structures were prepared using the same protocol to ensure consistent atom typing and charge assignment for subsequent core-constrained docking of the full AUTAC.

Docking of warhead and AUTAC. Docking was performed using the Schrödinger's Glide module in standard precision (SP) mode. For initial warhead docking, receptor grids were generated based on the prepared protein structures. In the case of MCL1, the grid was centered on the co-crystallized selective inhibitor S64315 to define the BH3-binding groove. Identical grid-generation parameters were subsequently applied to BCL2 and BCL-XL to ensure consistent treatment across targets. Docking of the isolated warhead was performed with 100 independent docking runs followed by post-docking minimization. The highest-ranked pose for each protein, based on GlideScore and consistency with canonical BH3-groove interactions, was selected as the reference warhead binding mode. Docking of the full AUTAC molecule was then carried out using a core-constrained protocol to preserve the validated warhead orientation. Atoms defining the rigid warhead pharmacophore were manually selected and constrained to overlay the reference warhead pose with an RMSD tolerance of 0.1 Å. Receptor grids were generated from the warhead-bound protein complexes, centered on the bound warhead and using identical grid dimensions and parameters for MCL1, BCL2, and BCL-XL. Enhanced conformational sampling was employed to allow flexibility of the linker and FBnG degradation tag, and fifty AUTAC poses were generated per target. All poses were subjected to post-docking minimization, ranked by GlideScore, and clustered to identify dominant binding families.

MM-GBSA binding energy calculations. Binding free energies of AUTAC–protein complexes were estimated using the Molecular Mechanics/Generalized Born Surface Area (MM-GBSA) method. MM-GBSA calculations were performed using the **OPLS4 force field** in combination with the **VSGB implicit solvent model**. Prior to energy evaluation, each protein–ligand complex

was subjected to restrained energy minimization to relieve local strain while preserving the docked geometry. Binding free energies (ΔG_bind) were computed as the difference between the minimized complex energy and the sum of the minimized energies of the isolated protein and ligand. The total binding free energy was decomposed into **van der Waals (ΔG_vdW)**, and **electrostatic (ΔG_electrostatic)** contributions. Average MM-GBSA values were reported as the mean of the top five poses for each target.

Solvent-accessible surface area (SASA) analysis of FBnG exposure. Molecular surfaces were generated using a **probe radius of 1.4 Å**, corresponding to a water molecule. For each target, the FBnG tag was explicitly selected, and its SASA was calculated in both the **isolated (free) state** and the **protein-bound complex** using identical surface generation parameters. FBnG exposure in the bound state was quantified as the absolute SASA and as a **fraction of the free-state SASA**. Differences in FBnG accessibility upon binding (ΔFBnG) were calculated as FBnG_free − FBnG_bound.

Statistical analysis and reporting. Unless otherwise indicated, data are presented as mean ± SEM from at least three independent biological replicates, each performed with technical triplicates (or six technical replicates for cell viability assays). Statistical analyses were performed using GraphPad Prism 10. Statistical significance of each condition compared to the indicated control or treatment was determined using unpaired, two-sided Student's t-tests or two-way ANOVA with Tukey's or Sidak's post hoc tests, as appropriate. A P value < 0.05 was considered statistically significant. Statistical significance levels are indicated in the figures as follows: *$P < 0.05$; **$P < 0.01$; ***$P < 0.001$; and ****$P < 0.0001$.

Data and Code Availability. No high-throughput sequencing or omics datasets requiring deposition were generated. Source data underlying figures are available from the corresponding author upon reasonable request.

No custom code was generated. Molecular docking was performed using Schrödinger software (Glide/LigPrep/Epik/MM-GBSA; OPLS4). Image analyses were performed in ImageJ; statistics and plots were generated in GraphPad Prism 10.

ACKNOWLEDGEMENTS

This work was supported by a NIH/NIGMS grant R01GM132396 (S.K.R). We thank Gugan Thuduppathy for helpful discussions. We thank Bin Hu, and Wang Li for their assistance with the mouse studies. Services and products in support of the research project were generated by the Virginia Commonwealth University Cancer Mouse Models Core Laboratory and Microscopy Shared Resource, supported, in part, with funding to the Massey Cancer Center from NIH-NCI Cancer Center Support Grant P30 CA016059.

CONFLICT OF INTEREST STATEMENT

The authors declare no conflict of interest.

DATA AVAILABILITY STATEMENT

All data that support the findings of this study are available from the corresponding author upon reasonable request.

FIGURE LEGENDS

Figure 1. AUTAC degrades Mcl1 through autophagy. (A) The chemical structure of Mcl1-specific AUTAC consists of a Mcl1 binding moiety connected to a FBnG-tag via a pyrazole linker. The second-generation AUTAC achieved superior degradative efficiency by overcoming the membrane permeability limitations associated with the negatively charged cyclic phosphate scaffold of the first-generation construct. **(B)** AUTAC binding in (B1) Mcl1, (B2) Bcl2 and (**3**) Bclxl. Mcl1 (PDB ID: 6YBL), Bcl2 (PDB ID: 2XA0) and Bclxl (PDB ID: 1R2D) are shown as grey, yellow and orange surfaces. Warhead, linker and FBnG tag are shown as salmon, green and cyan sticks respectively. **(C)** Western blot analysis for Mcl1, Bcl2, Bclxl, and LC3I/II proteins in U266B1 cells treated with the indicated concentrations of AUTAC for 24h and 48h. GAPDH was used as the loading control. **(D)** Western blot analysis for Mcl1 protein in U266B1 cells treated with AUTAC (5 μM), Mcl1 moiety (5 μM), FBnG (10 μM), as well as starved U266B1 cells for 24h. GAPDH was used as the loading control. **(E)** Western blot analysis for Mcl1, and LC3I/II proteins in U266B1 cells treated with different combinations of AUTAC (5 μM), CQ (20 μM) or 3-MA (1 mM) for 24h. GAPDH was used as the loading control. **(F)** Western blot analysis for ATG5, Mcl1, and LC3I/II proteins in U266B1 wild-type and U266B1 ATG5^{KD} cells treated with AUTAC (5 μM) for 24h. GAPDH was used as the loading control. **(G)**The percentage of cellular viability for U266B1 and RPMI-8226 cells treated with the indicated concentrations AUTAC for 24, 48 and 72h. **(H)** Western blot analysis for cleaved caspase 3 and cleaved PARP proteins in U266B1 cells treated with AUTAC (5 μM) for 24 and 48h. GAPDH was used as the loading control. **(I)** The percentage of cell death for U266B1 cells treated with AUTAC (5 μM) for 48 and 72h. **(J)** Western blot analysis for cleaved caspase 3 protein in U266B1 cells treated with AUTAC (5 μM), Mcl1 moiety (5 μM), FBnG (5 μM), as well as starved U266B1 cells for 24h. GAPDH was used as the loading control. **(K)** Western blot analysis of Mcl1 and Beclin1 in U266B1 cells treated with AUTAC (10 μM) for 24 h, followed by co-immunoprecipitation.

Three biological replicates for each cell line were used to perform cell viability assay and Western blotting. The uncropped blots are shown in the Supplemental Materials. Statistical significance of each condition compared to the indicated control or treatment was determined using unpaired Student's t-test or two-way ANOVA with Tukey or Sidak post hoc tests, as appropriate. Data are represented as mean ± SEM. Significance levels are indicated as follows: * $p < 0.05$, ** $p < 0.01$, *** $p < 0.001$ and **** $p < 0.0001$.

Figure 2. AUTAC selectively degrades Mcl1 via TRAF6/UBC13/p62(SQSTMI). (A) Confocal images for Mcl1, K63, p62/SQSTM1 and LC3B proteins in U266B1^{WT} cells treated with AUTAC (5 and 10 μM) for 24 (scale 10 μM). **(B)** Western blot analysis of Mcl1, K63, and p62/SQSTM1 in U266B1 cells treated with AUTAC (10 μM) for 16 h, followed by co-immunoprecipitation. **(C)** Confocal images for Mcl1, and LC3B proteins in U266B1p62^{KD} cells treated with AUTAC (5 and 10 μM) for 24 (scale 10 μM). **(D)** Western blot analysis for p62/SQSTM1, Mcl1 and cleaved PARP and cleaved caspase 3 proteins in U266B1^{WT} and U266B1 p62^{KD} cells treated with AUTAC (5 μM) for 24h. GAPDH was used as the loading control. **(E and F)** Western blot analysis for Mcl1, TRAF6, UBC13 and cleaved PARP proteins in U266B1^{WT}, U266B1 TRAF6 ^{KD}, and UBC13 ^{KD} treated with AUTAC (5 μM) for 24h.

GAPDH was used as the loading control. **(G)** The percentage of cell death for U266B1^{WT}, p62^{KD}, TRAF6^{KD}, and UBC13^{KD} cells treated with AUTAC (5 μM) for 72h.

Three biological replicates for each cell line were used to perform cell viability assay and Western blotting. The uncropped blots are shown in the Supplemental Materials. Statistical significance of each condition compared to the indicated control or treatment was determined using unpaired Student's t-test or two-way ANOVA with Tukey or Sidak post hoc tests, as appropriate. Data are represented as mean ± SEM. Significance levels are indicated as follows: * $p < 0.05$, ** $p < 0.01$, *** $p < 0.001$ and **** $p < 0.0001$.

Figure 3. Carfilzomib enhances AUTAC-mediated Mcl1 degradation in multiple myeloma and non-small cell lung cancer cells. (A) Western blot analysis for Mcl1, and LC3I/II proteins in U266B1, MM.1S, RPMI-8226 and AMO-1 cells treated with AUTAC (5 μM) and/or CFZ (10 nM) for 16h, except for AMO-1 cells treated for 24h. GAPDH was used as the loading control. **(B)** Western blot analysis for Mcl1, and LC3I/II proteins in U266B1^{R} and AMO-1^{R} cells treated with AUTAC (5 μM) for 48h, then CFZ (10 nM) was added for the last 24h. GAPDH was used as the loading control. **(C)** Western blot analysis for Mcl1, and LC3I/II proteins in NCI-H1975 and NCI-H1975^{R} cells treated with AUTAC (5 μM) and/or CFZ (2.5 nM, and 10 nM) for 72h. GAPDH was used as the loading control. **(D)** Western blot analysis for Mcl1, and LC3I/II proteins in U266B1 cells treated with the indicated concentrations of AUTAC and/or CFZ (10 nM) for 16h. GAPDH was used as the loading control. **(E and F)** Confocal images and their quantification for Mcl1, LC3B **(E)** and LAMP1 **(F)** proteins in U266B1 treated with AUTAC (5 μM) and/or CFZ (10 nM) for 16h (scale 10 μM).

Three biological replicates for each cell line were used to perform Western blotting. The uncropped blots are shown in the Supplemental Materials. Statistical significance of each condition compared to the indicated control or treatment was determined using unpaired Student's t-test or two-way ANOVA with Tukey or Sidak post hoc tests, as appropriate. Data are represented as mean ± SEM. Significance levels are indicated as follows: * $p < 0.05$, ** $p < 0.01$, *** $p < 0.001$ and **** $p < 0.0001$.

Figure 4. Carfilzomib-mediated potentiation of AUTAC activity is dependent on NRF1, p62/SQSTM1 and functional autophagy. (A) Western blot analysis for NRF1, Mcl1, cleaved PARP, cleaved caspase 3 and LC3I/II proteins in U266B1 ^{WT} and U266B1 NRF1^{KO} cell lines treated with AUTAC (5 μM) for 24h. GAPDH was used as the loading control. **(B)** The percentage of cellular viability for U266B1 ^{WT} and U266B1 NRF1^{KO} cell lines treated with AUTAC (5 μM) for 72h. **(C)** qRTPCR for the indicated genes in U266B1 ^{WT} and U266B1 NRF1^{KO} cell lines after treating with CFZ (20nM) for 20h. **(D)** Western blot analysis for NRF1, p62/SQSTM1, CTSD, GABARAPL1, and LAMP1 proteins in U266B1 ^{WT} and U266B1 NRF1^{KO} cell lines treated with CFZ (10 nM) for 16h. GAPDH was used as the loading control. **(E)** Western blot analysis for NRF1, and LC3II in U266B1 ^{WT} and U266B1 NRF1^{KO} cell lines after treating with CQ (20 μM), and/or CFZ (10 nM) for 16h. GAPDH was used as the loading control. **(F)** Western blot analysis for NRF1, Mcl1, and LC3I/II proteins in U266B1 ^{WT} and U266B1 NRF1^{KO} cell lines treated with AUTAC (5 μM) and/or CFZ (10 nM) for 16h. GAPDH was used as the loading control **(G)** Western blot analysis for ATG5, Mcl1, and LC3I/II proteins

in U266B1^{WT} and U266B1 ATG5 ^{KD} cell lines treated with AUTAC (5 μM) and/or CFZ (10 nM) for 16h. GAPDH was used as the loading control. **(H)** Western blot analysis for p62/SQSTM1, Mcl1, and LC3I/II proteins in U266B1^{WT} and U266B1 p62 ^{KD} cell lines treated with AUTAC (5 μM) and/or CFZ (10 nM) for 16h. GAPDH was used as the loading control.

Three biological replicates for each cell line were used to perform Western blotting. The uncropped blots are shown in the Supplemental Materials. Statistical significance of each condition compared to the indicated control or treatment was determined using unpaired Student's t-test or two-way ANOVA with Tukey or Sidak post hoc tests, as appropriate. Data are represented as mean ± SEM. Significance levels are indicated as follows: * $p < 0.05$, ** $p < 0.01$, *** $p < 0.001$ and **** $p < 0.0001$.

Figure 5. Carfilzomib in combination with AUTAC synergistically induces cell death in wild-type and proteasome inhibitor-resistant multiple myeloma cells. (A) The percentage of cellular viability for U266B1, MM.1S, AMO-1, RPMI-8226, U266B1^{R} and AMO-1^{R} cell lines treated with AUTAC (5 μM) for 72h, then the indicated concentrations of CFZ were added for the last 24h. The synergy between AUTAC and CFZ were determined using Bliss score. **(B)** Western blot analysis for cleaved caspase 3 protein in multiple myeloma cell lines after 16h (U266B1, MM.1S, RPMI-8226), and 24h (AMO-1) treatment with AUTAC (5 μM) and/or CFZ (10 nM), while U266B1^{R} and AMO-1^{R} cells treated for 48h with AUTAC (5 μM), then CFZ (10 nM) was added for the last 24h. GAPDH was used as the loading control. **(C)** The percentage of cellular viability for U266B1^{WT} and U266B1 p62^{KD} cell lines treated with AUTAC (5 μM) for 72h, then the indicated concentrations of CFZ were added for the last 24h.

Three biological replicates for each cell line were used to perform cell viability assay and Western blotting. In each independent replicate of synergy assays, a single well was used for each drug combination. The uncropped blots are shown in the Supplemental Materials. ns indicates non-statistical significance, while * $p < 0.05$, and **** $p < 0.0001$ indicates statistical significance of each condition compared to the indicated control/treatment as determined using two-way ANOVA with Sidak's post hoc test.

Figure 6. AUTAC potentiates the *in vivo* antitumor activity of CFZ in U266B1 xenograft models. (A) Tumor volumes of U266B1 xenografts following treatment with vehicle, CFZ (5 mg/kg), and/or AUTAC (50 mg/kg). CFZ was administered on days 1, 4, and 7, while AUTAC treatment was initiated on day 7 and continued daily. **(B)** Body weights of mice bearing U266B1 xenografts during treatment with vehicle, CFZ (5 mg/kg), and/or AUTAC (50 mg/kg). **(C)** Western blot analysis for Mcl1, Bcl2, Bclxl, p62/SQSTM1, and LC3II for U266B1 tumor xenografts from mice treated with vehicle, CFZ (5 mg/kg), and/or AUTAC (50 mg/kg). **(D)** The cell viability of U266B1 and AC16 cardiomyocytes treated with the indicated concentrations of AUTAC, S63845, AMG 176, UMI-77, AZD-5991, and A-1210477 for 72h with corresponding IC□□ values calculated for each cell line.

Three biological replicates for each cell line were used to perform Western blotting. The uncropped blots are shown in the Supplemental Materials. Statistical significance of each condition compared to the indicated control or treatment was determined using unpaired

Student's t-test or two-way ANOVA with Tukey or Sidak post hoc tests, as appropriate. Data are represented as mean ± SEM. Significance levels are indicated as follows: * $p < 0.05$, ** $p < 0.01$, *** $p < 0.001$ and **** $p < 0.0001$.

Figure 7. Classical Mcl1 inhibitors do not synergize with carfilzomib in inducing cell death in wild-type or proteasome inhibitor-resistant multiple myeloma cells. (A) The percentage of cellular viability for U266B1, and U266B1R cell lines treated with 5μM of S63845, AMG 176, UMI-77, AZD-5991, and A-1210477 for 72h, then the indicated concentrations of CFZ were added for the last 24h. The synergy between AUTAC and CFZ were determined using Bliss score.

Three biological replicates for each cell line were used to perform cell viability assay. In each independent replicate of the synergy assay, a single well was used for each drug combination.

Figure 8. The impact of combining carfilzomib with AUTAC in wild-type and proteasome inhibitor-resistant non-small cell lung cancer cells. (A) The percentage of cellular viability for NCI-H1975 and NCI-H1975^{R} cells treated with AUTAC (5 μM) and/or the indicated concentrations of CFZ for 72h. The synergy between AUTAC and CFZ were determined using Bliss score. **(B)** Western blot analysis for cleaved caspase 3 protein in NCI-H1975 and NCI-H1975^{R} cells treated with AUTAC (5 μM) and/or CFZ (2.5, and 10 nM) for 72h. GAPDH was used as the loading control. **(C)** Colony formation assay and its quantification for NCI-H1975 and NCI-H1975^{R} cells treated with AUTAC (5 μM) and/or CFZ (2.5, and 10 nM) for 72h, then supplemented with media every three days for total 9 days.

Three biological replicates for each cell line were used to perform cell viability assay, colony formation assay and Western blotting. In each independent replicate of the synergy assay, a single well was used for each drug combination. The uncropped blots are shown in the Supplemental Materials. ns indicates non-statistical significance, while ** $p < 0.01$, *** $p < 0.001$ and **** $p < 0.0001$ indicates statistical significance of each condition compared to the indicated control/treatment as determined using two-way ANOVA with Sidak's post hoc test.

Supplementary Figure 1. Structural comparison and docking of AUTAC warhead in Mcl1, Bcl2, and Bclxl. (A) Sequence alignment of human Mcl1, Bcl2 and Bclxl; **(B)** Structural overlay of Mcl1 vs Bcl2 vs Bclxl BH3- binding grooves. Mcl1 (PDB ID: 2PQK), Bcl2 (PDB ID: 2XA0), Bclxl (PDB ID 1R2D) and BH3-peptides are shown as grey, yellow, orange and salmon cartoons respectively. **(C)** Highest-ranked docking pose of the warhead in (**C1**) Mcl1, (**C2**) Bcl2, and (**C3**) Bclxl. Proteins are shown as cartoons (Mcl1 grey, Bcl2 yellow, Bclxl orange). The warhead is shown as salmon sticks. Key pocket residues are shown as sticks, and hydrogen-bonding interactions are indicated by dashed lines. **(D)** Representative florescence microscopy images and their quantification for U266B1 cells subjected to starvation for 24h, then the cells stained with DAPI and lysotracker stain. All images were generated under the same magnification (20X). **(E)** Western blot analysis for LC3I/II protein in U266B1 starved and treated with CQ (20 μM) for 24h. GAPDH was used as the loading control.

Three biological replicates for each cell line were used to perform Western blotting. The uncropped blots are shown in the Supplemental Materials.

Supplementary Figure 2. AUTAC promotes lysosomal and autophagic association of Mcl1 in U266B1 cells. (A) Western blot analysis for mTOR, p53, HSP70, HSP60, ERK, and ULK1 proteins in U266B1 treated with AUTAC 5 μM for 24h. GAPDH was used as the loading control. **(B)** Confocal images with their quantification for Mcl1, LAMP1 and LC3B proteins in U266B1 cells treated with AUTAC (5 μM) for 24 and 48h (scale 10 μM).

Three biological replicates for each cell line were used to perform Western blotting. The uncropped blots are shown in the Supplemental Materials. Statistical significance of each condition compared to the indicated control or treatment was determined using unpaired Student's t-test or two-way ANOVA with Tukey or Sidak post hoc tests, as appropriate. Data are represented as mean ± SEM. Significance levels are indicated as follows: * $p < 0.05$, ** $p < 0.01$, *** $p < 0.001$ and **** $p < 0.0001$.

Supplementary Figure 3. AUTAC selectively degrades Mcl1 and subsequently induces autophagy through a Beclin1–dependent axis.(A) Western blot analysis for Mcl1, and LC3I/II proteins in U266B1 treated with Mcl1 AUTAC (5μM) or MetAP2 AUTAC (10μM) for 24h. GAPDH was used as the loading control. **(B)** Western blot analysis for LC3I/II protein in U266B1 treated with CQ (20 μM) and/or Mcl1 AUTAC (5μM) or MetAP2 AUTAC (10μM) for 24h. GAPDH was used as the loading control. **(C)** Western blot analysis for Mcl1, mTOR, p-mTOR, T-S6, and p-S6 proteins in U266B1 treated with Mcl1 AUTAC (5μM) and rapamycin (100nM) for 24h. GAPDH was used as the loading control. **(D)** Western blot analysis for LC3I/II protein in U266B1 treated with CQ (20 μM) and/or Mcl1 AUTAC (5μM), or rapamycin (100nM) for 24h. GAPDH was used as the loading control. **(E)** Western blot analysis for LC3I/II protein in U266B1 treated with CQ (20 μM) and/or Mcl1 moiety (10μM), or FBNG (10μM) for 24h. GAPDH was used as the loading control. **(F)** Western blot analysis for Mcl1, and LC3I/II proteins in U266B1^{WT}, and U266B1 Mcl1 ^{KD} treated with CQ (20 μM) and/or AUTAC (5μM) for 24h. GAPDH was used as the loading control. **(G)** Western blot analysis for LC3I/II protein in U266B1 treated with CQ (20 μM), AUTAC (5 μM), and N-acetyl cysteine (NAC) (0.5 μM) for 24h. GAPDH was used as the loading control. **(H)** Western blot analysis for Beclin1, and p-Beclin1 (Ser15) proteins in U266B1 treated with AUTAC (5 μM) for 24h. GAPDH was used as the loading control.

Three biological replicates for each cell line were used to perform Western blotting. The uncropped blots are shown in the Supplemental Materials.

Supplementary Figure 4. Autophagy induction via starvation augments the Mcl1 degradation ability of AUTAC. (A) Western blot analysis for Mcl1 protein in U266B1 treated with AUTAC (5 μM), NSC697923 (1μM) and/or C25-140 (10 and 30 μM) for 24h. GAPDH was used as the loading control. **(B)** Western blot analysis for p62, Mcl1, and LC3I/II proteins in

U266B1 starved and treated with AUTAC (5 μM) for 24h. GAPDH was used as the loading control.

Three biological replicates for each cell line were used to perform Western blotting. The uncropped blots are shown in the Supplemental Materials.

Supplementary Figure 5. Carfilzomib induces a cytoprotective autophagy in multiple myeloma cells. (A) Representative florescence microscopy images with their quantification for U266B1 cells treated with carfilzomib (10 nM) for 24h, then the cells stained with DAPI and lysotracker stain. All images were generated under the same magnification (20X). **(B)** Western blot analysis for LC3I/II protein in MM.1S and RPMI-8226 cells treated with carfilzomib (10 nM) and/or CQ (20 μM) for 16h. GAPDH was used as the loading control. **(C)** Western blot analysis for LC3I/II protein in U266B1 and U266B1^{R} treated with carfilzomib (10 nM) and/or CQ (20 μM) or bafilomycin (10 nM) for 24h. GAPDH was used as the loading control. **(D and E)** The percentage of cellular viability for **(D)** U266B1 and **(E)** U266B1^{R} cells treated with CQ (20 μM) or bafilomycin (10 nM) for 72h, then the indicated concentrations of CFZ were added for the last 24h. The synergy between CQ, or BAF and CFZ were determined using Bliss score.

Three biological replicates for each cell line were used to perform cell viability assay, and Western blotting. In each independent replicate of the synergy assay, a single well was used for each drug combination. The uncropped blots are shown in the Supplemental Materials. ns indicates non-statistical significance, while **** $p < 0.0001$ indicates statistical significance of each condition compared to the indicated control/treatment as determined using two-way ANOVA with Sidak's post hoc test.

Supplementary Figure 6. Mcl1 contributes to proteasome inhibitor resistance in multiple myeloma cells. (A) Viability of U266B1^{WT}, U266B1^{R}, and U266B1 Mcl1 overexpression (OE) cells treated with the indicated concentrations of CFZ for 24h. **(B)** Western blot analysis for Mcl1 protein in U266B1^{WT}, U266B1^{R}, and U266B1 Mcl1 ^{OE}. GAPDH was used as the loading control. **(C)** Western blot analysis for Mcl1, LC3I/II, cleaved PARP, and cleaved caspase 3 proteins in U266B1^{WT} and U266B1 Mcl1^{OE} cells treated with AUTAC (5 μM) for 48h, then CFZ (10 nM) was added for the last 24h. GAPDH was used as the loading control. **(D)** The percentage of cellular viability for U266B1^{WT} and U266B1 Mcl1^{OE} cells treated with AUTAC (5 μM) for 72h, then the indicated concentrations of CFZ were added for the last 24h.

Three biological replicates for each cell line were used to perform cell viability assay, and Western blotting. The uncropped blots are shown in the Supplemental Materials.

REFERENCES

1 Moreau, P. *et al.* Proteasome inhibitors in multiple myeloma: 10 years later. *Blood* **120**, 947-959, doi:10.1182/blood-2012-04-403733 (2012).

2 Lee, H. J., Badillo, M., Romaguera, J. & Wang, M. A phase II study of carfilzomib in the treatment of relapsed/refractory mantle cell lymphoma. *British journal of haematology* **184**, 460-462, doi:10.1111/bjh.15107 (2019).

3 Patiño-Escobar, B., Talbot, A. & Wiita, A. P. Overcoming proteasome inhibitor resistance in the immunotherapy era. *Trends in pharmacological sciences* **44**, 507-518, doi:10.1016/j.tips.2023.05.006 (2023).

4 Ito, S. Proteasome Inhibitors for the Treatment of Multiple Myeloma. *Cancers* **12**, doi:10.3390/cancers12020265 (2020).

5 Gu, J. J. *et al.* The novel proteasome inhibitor carfilzomib induces cell cycle arrest, apoptosis and potentiates the anti-tumour activity of chemotherapy in rituximab-resistant lymphoma. *British journal of haematology* **162**, 657-669, doi:10.1111/bjh.12452 (2013).

6 Weyburne, E. S. *et al.* Inhibition of the Proteasome β2 Site Sensitizes Triple-Negative Breast Cancer Cells to β5 Inhibitors and Suppresses Nrf1 Activation. *Cell chemical biology* **24**, 218-230, doi:10.1016/j.chembiol.2016.12.016 (2017).

7 Shah, M. A. *et al.* A multicenter, phase II study of bortezomib (PS-341) in patients with unresectable or metastatic gastric and gastroesophageal junction adenocarcinoma. *Investigational new drugs* **29**, 1475-1481, doi:10.1007/s10637-010-9474-7 (2011).

8 Rosenberg, J. E. *et al.* Phase II study of bortezomib in patients with previously treated advanced urothelial tract transitional cell carcinoma: CALGB 90207. *Annals of oncology : official journal of the European Society for Medical Oncology* **19**, 946-950, doi:10.1093/annonc/mdm600 (2008).

9 Papadopoulos, K. P. *et al.* A phase I/II study of carfilzomib 2-10-min infusion in patients with advanced solid tumors. *Cancer chemotherapy and pharmacology* **72**, 861-868, doi:10.1007/s00280-013-2267-x (2013).

10 Aghajanian, C. *et al.* A phase II evaluation of bortezomib in the treatment of recurrent platinum-sensitive ovarian or primary peritoneal cancer: a Gynecologic Oncology Group study. *Gynecologic oncology* **115**, 215-220, doi:10.1016/j.ygyno.2009.07.023 (2009).

11 Engel, R. H. *et al.* A phase II study of single agent bortezomib in patients with metastatic breast cancer: a single institution experience. *Cancer investigation* **25**, 733-737, doi:10.1080/07357900701506573 (2007).

12 Ge, M. *et al.* Modulating proteasome inhibitor tolerance in multiple myeloma: an alternative strategy to reverse inevitable resistance. *British Journal of Cancer* **124**, 770-776, doi:10.1038/s41416-020-01191-y (2021).

13 Ward, M. A. *et al.* Transcription factor Nrf1 regulates proteotoxic stress-induced autophagy. *The Journal of cell biology* **223**, doi:10.1083/jcb.202306150 (2024).

14 Koizumi, S. *et al.* The aspartyl protease DDI2 activates Nrf1 to compensate for proteasome dysfunction. *eLife* **5**, doi:10.7554/eLife.18357 (2016).

15 Lehrbach, N. J. & Ruvkun, G. Proteasome dysfunction triggers activation of SKN-1A/Nrf1 by the aspartic protease DDI-1. *eLife* **5**, doi:10.7554/eLife.17721 (2016).

16 Wirawan, E., Berghe, T. V., Lippens, S., Agostinis, P. & Vandenabeele, P. Autophagy: for better or for worse. *Cell Research* **22**, 43-61, doi:10.1038/cr.2011.152 (2012).

17 Elshazly, A. M., Wright, P. A., Xu, J. & Gewirtz, D. A. Topoisomerase I poisons-induced autophagy: Cytoprotective, Cytotoxic or Non-protective. *Autophagy reports* **2**, 1-16, doi:10.1080/27694127.2022.2155904 (2023).

1119 18 Jarauta, V. *et al.* Inhibition of autophagy with chloroquine potentiates carfilzomib-induced
1120 apoptosis in myeloma cells in vitro and in vivo. *Cancer letters* **382**, 1-10,
1121 doi:10.1016/j.canlet.2016.08.019 (2016).
1122 19 Riz, I., Hawley, T. S. & Hawley, R. G. KLF4-SQSTM1/p62-associated prosurvival autophagy
1123 contributes to carfilzomib resistance in multiple myeloma models. *Oncotarget* **6**, 14814-14831,
1124 doi:10.18632/oncotarget.4530 (2015).
1125 20 Chavda, S. J. *et al.* Autophagy Blockade Disrupts Myeloma Cell Recovery from Proteasome
1126 Inhibition and Enhances Apoptosis. *Blood* **138**, 1567, doi:https://doi.org/10.1182/blood-2021-
1127 146400 (2021).
1128 21 Salimi, A. *et al.* Targeting autophagy increases the efficacy of proteasome inhibitor treatment in
1129 multiple myeloma by induction of apoptosis and activation of JNK. *BMC Cancer* **22**, 735,
1130 doi:10.1186/s12885-022-09775-y (2022).
1131 22 Ito, C. *et al.* Endogenous nitrated nucleotide is a key mediator of autophagy and innate defense
1132 against bacteria. *Mol Cell* **52**, 794-804, doi:10.1016/j.molcel.2013.10.024 (2013).
1133 23 Takahashi, D. *et al.* AUTACs: Cargo-Specific Degraders Using Selective Autophagy. *Molecular Cell*
1134 **76**, 797-810.e710, doi:10.1016/j.molcel.2019.09.009 (2019).
1135 24 Wang, H., Guo, M., Wei, H. & Chen, Y. Targeting MCL-1 in cancer: current status and
1136 perspectives. *Journal of Hematology & Oncology* **14**, 67, doi:10.1186/s13045-021-01079-1
1137 (2021).
1138 25 Lucendo, E. *et al.* Mcl-1 and Bok transmembrane domains: Unexpected players in the
1139 modulation of apoptosis. *Proceedings of the National Academy of Sciences* **117**, 27980-27988,
1140 doi:doi:10.1073/pnas.2008885117 (2020).
1141 26 Al-Odat, O. *et al.* Mcl-1 Inhibition: Managing Malignancy in Multiple Myeloma. *Frontiers in*
1142 *pharmacology* **12**, 699629, doi:10.3389/fphar.2021.699629 (2021).
1143 27 Tron, A. E. *et al.* Discovery of Mcl-1-specific inhibitor AZD5991 and preclinical activity in multiple
1144 myeloma and acute myeloid leukemia. *Nature Communications* **9**, 5341, doi:10.1038/s41467-
1145 018-07551-w (2018).
1146 28 Zhou, W. *et al.* Small interfering RNA targeting mcl-1 enhances proteasome inhibitor-induced
1147 apoptosis in various solid malignant tumors. *BMC Cancer* **11**, 485, doi:10.1186/1471-2407-11-
1148 485 (2011).
1149 29 Nencioni, A. *et al.* Evidence for a protective role of Mcl-1 in proteasome inhibitor-induced
1150 apoptosis. *Blood* **105**, 3255-3262, doi:https://doi.org/10.1182/blood-2004-10-3984 (2005).
1151 30 Al-Odat, O. S. *et al.* KS18, a Mcl-1 inhibitor, improves the effectiveness of bortezomib and
1152 overcomes resistance in refractory multiple myeloma by triggering intrinsic apoptosis. *Frontiers*
1153 *in pharmacology* **15**, 1436786, doi:10.3389/fphar.2024.1436786 (2024).
1154 31 Ponder, K. G. *et al.* Dual inhibition of Mcl-1 by the combination of carfilzomib and TG02 in
1155 multiple myeloma. *Cancer biology & therapy* **17**, 769-777, doi:10.1080/15384047.2016.1192086
1156 (2016).
1157 32 Bolomsky, A. *et al.* Heterogeneous modulation of Bcl-2 family members and drug efflux mediate
1158 MCL-1 inhibitor resistance in multiple myeloma. *Blood advances* **5**, 4125-4139,
1159 doi:10.1182/bloodadvances.2020003826 (2021).
1160 33 Bolomsky, A. *et al.* MCL-1 inhibitors, fast-lane development of a new class of anti-cancer agents.
1161 *Journal of Hematology & Oncology* **13**, 173, doi:10.1186/s13045-020-01007-9 (2020).
1162 34 Takahashi, D. *et al.* Second-Generation AUTACs for Targeted Autophagic Degradation. *Journal of*
1163 *medicinal chemistry* **66**, 12342-12372, doi:10.1021/acs.jmedchem.3c00861 (2023).
1164 35 Wang, Z. *et al.* Proteolysis Targeting Chimeras for the Selective Degradation of Mcl-1/Bcl-2
1165 Derived from Nonselective Target Binding Ligands. *Journal of medicinal chemistry* **62**, 8152-
1166 8163, doi:10.1021/acs.jmedchem.9b00919 (2019).

1167 36 Friesner, R. A. *et al.* Glide: a new approach for rapid, accurate docking and scoring. 1. Method
1168 and assessment of docking accuracy. *Journal of medicinal chemistry* **47**, 1739-1749,
1169 doi:10.1021/jm0306430 (2004).
1170 37 Halgren, T. A. *et al.* Glide: a new approach for rapid, accurate docking and scoring. 2. Enrichment
1171 factors in database screening. *Journal of medicinal chemistry* **47**, 1750-1759,
1172 doi:10.1021/jm030644s (2004).
1173 38 Szlavik, Z. *et al.* Discovery of S64315, a Potent and Selective Mcl-1 Inhibitor. *Journal of medicinal*
1174 *chemistry* **63**, 13762-13795, doi:10.1021/acs.jmedchem.0c01234 (2020).
1175 39 Ku, B., Liang, C., Jung, J. U. & Oh, B. H. Evidence that inhibition of BAX activation by BCL-2
1176 involves its tight and preferential interaction with the BH3 domain of BAX. *Cell Res* **21**, 627-641,
1177 doi:10.1038/cr.2010.149 (2011).
1178 40 Manion, M. K. *et al.* Bcl-XL mutations suppress cellular sensitivity to antimycin A. *The Journal of*
1179 *biological chemistry* **279**, 2159-2165, doi:10.1074/jbc.M306021200 (2004).
1180 41 Stamelos, V. A., Redman, C. W. & Richardson, A. Understanding sensitivity to BH3 mimetics:
1181 ABT-737 as a case study to foresee the complexities of personalized medicine. *Journal of*
1182 *molecular signaling* **7**, 12, doi:10.1186/1750-2187-7-12 (2012).
1183 42 Yi, J. *et al.* Characterizing the consensus residue specificity and surface of BCL-2 binding to BH3
1184 ligands using the Knob-Socket model. *PloS one* **18**, e0281463,
1185 doi:10.1371/journal.pone.0281463 (2023).
1186 43 Kim, J. *et al.* Leveraging the Fragment Molecular Orbital and MM-GBSA Methods in Virtual
1187 Screening for the Discovery of Novel Non-Covalent Inhibitors Targeting the TEAD Lipid Binding
1188 Pocket. *International journal of molecular sciences* **25**, doi:10.3390/ijms25105358 (2024).
1189 44 Durham, E., Dorr, B., Woetzel, N., Staritzbichler, R. & Meiler, J. Solvent accessible surface area
1190 approximations for rapid and accurate protein structure prediction. *Journal of molecular*
1191 *modeling* **15**, 1093-1108, doi:10.1007/s00894-009-0454-9 (2009).
1192 45 Feng, Y., He, D., Yao, Z. & Klionsky, D. J. The machinery of macroautophagy. *Cell Research* **24**, 24-
1193 41, doi:10.1038/cr.2013.168 (2014).
1194 46 Hibshman, J. D. *et al.* Nonselective autophagy reduces mitochondrial content during starvation
1195 in Caenorhabditis elegans. *American Journal of Physiology-Cell Physiology* **315**, C781-C792,
1196 doi:10.1152/ajpcell.00109.2018 (2018).
1197 47 Huang, H. *et al.* Bulk RNA degradation by nitrogen starvation-induced autophagy in yeast. *The*
1198 *EMBO journal* **34**, 154-168, doi:10.15252/embj.201489083 (2015).
1199 48 Mauthe, M. *et al.* Chloroquine inhibits autophagic flux by decreasing autophagosome-lysosome
1200 fusion. *Autophagy* **14**, 1435-1455, doi:10.1080/15548627.2018.1474314 (2018).
1201 49 Seglen, P. O. & Gordon, P. B. 3-Methyladenine: specific inhibitor of autophagic/lysosomal
1202 protein degradation in isolated rat hepatocytes. *Proceedings of the National Academy of*
1203 *Sciences* **79**, 1889-1892 (1982).
1204 50 Demelash, A., Pfannenstiel, L. W., Liu, L. & Gastman, B. R. Mcl-1 regulates reactive oxygen
1205 species via NOX4 during chemotherapy-induced senescence. *Oncotarget* **8**, 28154-28168,
1206 doi:10.18632/oncotarget.15962 (2017).
1207 51 Chang, S. H. *et al.* The Protective Effects of Mcl-1 on Mitochondrial Damage and Oxidative Stress
1208 in Imiquimod-Induced Cancer Cell Death. *Cancers* **16**, doi:10.3390/cancers16173060 (2024).
1209 52 Scherz-Shouval, R. *et al.* Reactive oxygen species are essential for autophagy and specifically
1210 regulate the activity of Atg4. *The EMBO journal* **26**, 1749-1760-1760,
1211 doi:https://doi.org/10.1038/sj.emboj.7601623 (2007).
1212 53 Redza-Dutordoir, M. & Averill-Bates, D. A. Interactions between reactive oxygen species and
1213 autophagy: Special issue: Death mechanisms in cellular homeostasis. *Biochimica et biophysica*
1214 *acta. Molecular cell research* **1868**, 119041, doi:10.1016/j.bbamcr.2021.119041 (2021).

1215 54 Germain, M. *et al.* MCL-1 is a stress sensor that regulates autophagy in a developmentally
1216 regulated manner. *The EMBO journal* **30**, 395-407, doi:10.1038/emboj.2010.327 (2011).
1217 55 Elgendy, M. *et al.* Beclin 1 restrains tumorigenesis through Mcl-1 destabilization in an
1218 autophagy-independent reciprocal manner. *Nature Communications* **5**, 5637,
1219 doi:10.1038/ncomms6637 (2014).
1220 56 Halasi, M. *et al.* ROS inhibitor N-acetyl-L-cysteine antagonizes the activity of proteasome
1221 inhibitors. *The Biochemical journal* **454**, 201-208, doi:10.1042/bj20130282 (2013).
1222 57 Seibenhener, M. L. *et al.* Sequestosome 1/p62 is a polyubiquitin chain binding protein involved
1223 in ubiquitin proteasome degradation. *Molecular and cellular biology* **24**, 8055-8068,
1224 doi:10.1128/mcb.24.18.8055-8068.2004 (2004).
1225 58 Zaffagnini, G. *et al.* p62 filaments capture and present ubiquitinated cargos for autophagy. *The*
1226 *EMBO journal* **37**, e98308, doi:https://doi.org/10.15252/embj.201798308 (2018).
1227 59 Ichimura, Y. *et al.* Structural Basis for Sorting Mechanism of p62 in Selective Autophagy*. *Journal*
1228 *of Biological Chemistry* **283**, 22847-22857, doi:https://doi.org/10.1074/jbc.M802182200 (2008).
1229 60 Lippai, M. & Lőw, P. The role of the selective adaptor p62 and ubiquitin-like proteins in
1230 autophagy. *BioMed research international* **2014**, 832704, doi:10.1155/2014/832704 (2014).
1231 61 Choi, Y. B. & Harhaj, E. W. HTLV-1 tax stabilizes MCL-1 via TRAF6-dependent K63-linked
1232 polyubiquitination to promote cell survival and transformation. *PLoS Pathog* **10**, e1004458,
1233 doi:10.1371/journal.ppat.1004458 (2014).
1234 62 Brenke, J. K. *et al.* Targeting TRAF6 E3 ligase activity with a small-molecule inhibitor combats
1235 autoimmunity. *The Journal of biological chemistry* **293**, 13191-13203,
1236 doi:10.1074/jbc.RA118.002649 (2018).
1237 63 Cheng, J. *et al.* A small-molecule inhibitor of UBE2N induces neuroblastoma cell death via
1238 activation of p53 and JNK pathways. *Cell death & disease* **5**, e1079, doi:10.1038/cddis.2014.54
1239 (2014).
1240 64 Shang, L. *et al.* Nutrient starvation elicits an acute autophagic response mediated by Ulk1
1241 dephosphorylation and its subsequent dissociation from AMPK. *Proceedings of the National*
1242 *Academy of Sciences of the United States of America* **108**, 4788-4793,
1243 doi:10.1073/pnas.1100844108 (2011).
1244 65 Fostier, K., De Becker, A. & Schots, R. Carfilzomib: a novel treatment in relapsed and refractory
1245 multiple myeloma. *OncoTargets and therapy* **5**, 237-244, doi:10.2147/ott.S28911 (2012).
1246 66 Zang, Y. *et al.* The next generation proteasome inhibitors carfilzomib and oprozomib activate
1247 prosurvival autophagy via induction of the unfolded protein response and ATF4. *Autophagy* **8**,
1248 1873-1874, doi:10.4161/auto.22185 (2012).
1249 67 Mizushima, N. & Yoshimori, T. How to interpret LC3 immunoblotting. *Autophagy* **3**, 542-545,
1250 doi:10.4161/auto.4600 (2007).
1251 68 Radhakrishnan, S. K. *et al.* Transcription factor Nrf1 mediates the proteasome recovery pathway
1252 after proteasome inhibition in mammalian cells. *Mol Cell* **38**, 17-28,
1253 doi:10.1016/j.molcel.2010.02.029 (2010).
1254 69 Radhakrishnan, S. K., den Besten, W. & Deshaies, R. J. p97-dependent retrotranslocation and
1255 proteolytic processing govern formation of active Nrf1 upon proteasome inhibition. *eLife* **3**,
1256 e01856 (2014).
1257 70 Vangala, J. R. & Radhakrishnan, S. K. Nrf1-mediated transcriptional regulation of the proteasome
1258 requires a functional TIP60 complex. *The Journal of biological chemistry* **294**, 2036-2045,
1259 doi:10.1074/jbc.RA118.006290 (2019).
1260 71 Vangala, J. R., Sotzny, F., Krüger, E., Deshaies, R. J. & Radhakrishnan, S. K. Nrf1 can be processed
1261 and activated in a proteasome-independent manner. *Current biology : CB* **26**, R834-r835,
1262 doi:10.1016/j.cub.2016.08.008 (2016).

1263 72 Bai, Z. *et al.* Autophagy and cancer treatment: four functional forms of autophagy and their
1264 therapeutic applications. *Journal of Zhejiang University. Science. B* **23**, 89-101,
1265 doi:10.1631/jzus.B2100804 (2022).
1266 73 Gewirtz, D. A. The four faces of autophagy: implications for cancer therapy. *Cancer research* **74**,
1267 647-651, doi:10.1158/0008-5472.Can-13-2966 (2014).
1268 74 Elshazly, A. M. *et al.* Is Autophagy Targeting a Valid Adjuvant Strategy in Conjunction with
1269 Tyrosine Kinase Inhibitors? *Cancers* **16**, 2989 (2024).
1270 75 Torka, P. *et al.* AMG176, an MCL-1 inhibitor, is active in pre-clinical models of aggressive B-cell
1271 lymphomas. *Leukemia & lymphoma* **64**, 1175-1185, doi:10.1080/10428194.2023.2200876
1272 (2023).
1273 76 Wong, K. Y. & Chim, C. S. Venetoclax, bortezomib and S63845, an MCL1 inhibitor, in multiple
1274 myeloma. *The Journal of pharmacy and pharmacology* **72**, 728-737, doi:10.1111/jphp.13240
1275 (2020).
1276 77 Galas-Filipowicz, D. *et al.* Co-operation of MCL-1 and BCL-X(L) anti-apoptotic proteins in stromal
1277 protection of MM cells from carfilzomib mediated cytotoxicity. *Frontiers in oncology* **14**,
1278 1394393, doi:10.3389/fonc.2024.1394393 (2024).
1279 78 Caenepeel, S. *et al.* AMG 176, a Selective MCL1 Inhibitor, Is Effective in Hematologic Cancer
1280 Models Alone and in Combination with Established Therapies. *Cancer discovery* **8**, 1582-1597,
1281 doi:10.1158/2159-8290.Cd-18-0387 (2018).
1282 79 Manasanch, E. E. & Orlowski, R. Z. Proteasome inhibitors in cancer therapy. *Nature reviews.*
1283 *Clinical oncology* **14**, 417-433, doi:10.1038/nrclinonc.2016.206 (2017).
1284 80 Nakagawa, I. *et al.* Autophagy defends cells against invading group A Streptococcus. *Science* **306**,
1285 1037-1040 (2004).
1286 81 Sawa, T. *et al.* Protein S-guanylation by the biological signal 8-nitroguanosine 3′, 5′-cyclic
1287 monophosphate. *Nature chemical biology* **3**, 727-735 (2007).
1288 82 Lu, S.-L. *et al.* Endothelial cells are intrinsically defective in xenophagy of Streptococcus
1289 pyogenes. *PLoS pathogens* **13**, e1006444 (2017).
1290 83 Tai, W. T. *et al.* Mcl-1-dependent activation of Beclin 1 mediates autophagic cell death induced
1291 by sorafenib and SC-59 in hepatocellular carcinoma cells. *Cell death & disease* **4**, e485,
1292 doi:10.1038/cddis.2013.18 (2013).
1293 84 Sharma, A. *et al.* BECN1 and BIM interactions with MCL-1 determine fludarabine resistance in
1294 leukemic B cells. *Cell death & disease* **4**, e628-e628, doi:10.1038/cddis.2013.155 (2013).
1295 85 Takahashi, D. & Arimoto, H. Targeting selective autophagy by AUTAC degraders. *Autophagy* **16**,
1296 765-766, doi:10.1080/15548627.2020.1718362 (2020).
1297 86 Yamada, A., Hikichi, M., Nozawa, T. & Nakagawa, I. FBXO2/SCF ubiquitin ligase complex directs
1298 xenophagy through recognizing bacterial surface glycan. *EMBO reports* **22**, e52584,
1299 doi:https://doi.org/10.15252/embr.202152584 (2021).
1300 87 Senichkin, V. V., Streletskaia, A. Y., Gorbunova, A. S., Zhivotovsky, B. & Kopeina, G. S. Saga of
1301 Mcl-1: regulation from transcription to degradation. *Cell death and differentiation* **27**, 405-419,
1302 doi:10.1038/s41418-019-0486-3 (2020).
1303 88 Sancho, M., Leiva, D., Lucendo, E. & Orzáez, M. Understanding MCL1: from cellular function and
1304 regulation to pharmacological inhibition. *The FEBS journal* **289**, 6209-6234,
1305 doi:10.1111/febs.16136 (2022).
1306 89 Tang, G. L. Q., Lai, J. X. H. & Pervaiz, S. Ubiquitin-proteasome pathway-mediated regulation of
1307 the Bcl-2 family: effects and therapeutic approaches. *Haematologica* **109**, 33-43,
1308 doi:10.3324/haematol.2023.283730 (2024).
1309 90 Cao, L., Liu, X., Zheng, B., Xing, C. & Liu, J. Role of K63-linked ubiquitination in cancer. *Cell death*
1310 *discovery* **8**, 410, doi:10.1038/s41420-022-01204-0 (2022).

1311 91 Roberts, J. Z., Crawford, N. & Longley, D. B. The role of Ubiquitination in Apoptosis and
1312 Necroptosis. *Cell Death & Differentiation* **29**, 272-284, doi:10.1038/s41418-021-00922-9 (2022).
1313 92 Wang, G. *et al.* K63-linked ubiquitination in kinase activation and cancer. *Frontiers in oncology* **2**,
1314 5, doi:10.3389/fonc.2012.00005 (2012).
1315 93 Zhou, Z. *et al.* K63 ubiquitin chains target NLRP3 inflammasome for autophagic degradation in
1316 ox-LDL-stimulated THP-1 macrophages. *Aging* **12**, 1747-1759, doi:10.18632/aging.102710
1317 (2020).
1318 94 Richard, T. J. C. *et al.* K63-linked ubiquitylation induces global sequestration of mitochondria. *Sci*
1319 *Rep* **10**, 22334, doi:10.1038/s41598-020-78845-7 (2020).
1320 95 Madiraju, C., Novack, J. P., Reed, J. C. & Matsuzawa, S. I. K63 ubiquitination in immune signaling.
1321 *Trends in immunology* **43**, 148-162, doi:10.1016/j.it.2021.12.005 (2022).
1322 96 Branigan, E., Plechanovová, A., Jaffray, E. G., Naismith, J. H. & Hay, R. T. Structural basis for the
1323 RING-catalyzed synthesis of K63-linked ubiquitin chains. *Nature structural & molecular biology*
1324 **22**, 597-602, doi:10.1038/nsmb.3052 (2015).
1325 97 Dósa, A. & Csizmadia, T. The role of K63-linked polyubiquitin in several types of autophagy.
1326 *Biologia Futura* **73**, 137-148, doi:10.1007/s42977-022-00117-4 (2022).
1327 98 Elshazly, A. M. & Gewirtz, D. A. Is Autophagy Inhibition in Combination with Temozolomide a
1328 Therapeutically Viable Strategy? *Cells* **12**, doi:10.3390/cells12040535 (2023).
1329 99 Manzo, C., Gareri, P. & Castagna, A. Psychomotor Agitation Following Treatment with
1330 Hydroxychloroquine. *Drug safety - case reports* **4**, 6, doi:10.1007/s40800-017-0048-x (2017).
1331 100 Xu, H., Zhang, X. Y., Wang, W. W. & Wang, J. Hydroxychloroquine Increased Anxiety-Like
1332 Behaviors and Disrupted the Expression of Some Related Genes in the Mouse Brain. *Frontiers in*
1333 *pharmacology* **12**, 633112, doi:10.3389/fphar.2021.633112 (2021).
1334 101 Naddaf, E., Paul, P. & AbouEzzeddine, O. F. Chloroquine and Hydroxychloroquine Myopathy:
1335 Clinical Spectrum and Treatment Outcomes. *Frontiers in neurology* **11**, 616075,
1336 doi:10.3389/fneur.2020.616075 (2020).
1337 102 Chougoni, K. K. *et al.* Oncogenic Mutant p53 Sensitizes Non–Small Cell Lung Cancer Cells to
1338 Proteasome Inhibition via Oxidative Stress–Dependent Induction of Mitochondrial Apoptosis.
1339 *Cancer Research Communications* **4**, 2685-2698, doi:10.1158/2767-9764.Crc-23-0637 (2024).
1340 103 Li, L. *et al.* Non-canonical role for the ataxia-telangiectasia-Rad3 pathway in STAT3 activation in
1341 human multiple myeloma cells. *Cellular oncology (Dordrecht, Netherlands)* **46**, 1369-1380,
1342 doi:10.1007/s13402-023-00817-6 (2023).
1343 104 Chen, S. *et al.* Targeting SQSTM1/p62 induces cargo loading failure and converts autophagy to
1344 apoptosis via NBK/Bik. *Molecular and cellular biology* **34**, 3435-3449, doi:10.1128/mcb.01383-13
1345 (2014).
1346 105 Euhus, D. M., Hudd, C., Laregina, M. C. & Johnson, F. E. Tumor measurement in the nude mouse.
1347 *Journal of surgical oncology* **31**, 229-234 (1986).
1348 106 Zheng, S. *et al.* SynergyFinder Plus: Toward Better Interpretation and Annotation of Drug
1349 Combination Screening Datasets. *Genomics, proteomics & bioinformatics* **20**, 587-596,
1350 doi:10.1016/j.gpb.2022.01.004 (2022).
1351 107 Strober, W. Trypan Blue Exclusion Test of Cell Viability. *Current protocols in immunology* **111**,
1352 A3.B.1-a3.B.3, doi:10.1002/0471142735.ima03bs111 (2015).
1353 108 Sastry, G. M., Adzhigirey, M., Day, T., Annabhimoju, R. & Sherman, W. Protein and ligand
1354 preparation: parameters, protocols, and influence on virtual screening enrichments. *Journal of*
1355 *computer-aided molecular design* **27**, 221-234, doi:10.1007/s10822-013-9644-8 (2013).
1356 109 Johnston, R. C. *et al.* Epik: pK(a) and Protonation State Prediction through Machine Learning.
1357 *Journal of chemical theory and computation* **19**, 2380-2388, doi:10.1021/acs.jctc.3c00044
1358 (2023).

110 Lu, C. *et al.* OPLS4: Improving Force Field Accuracy on Challenging Regimes of Chemical Space. *Journal of chemical theory and computation* **17**, 4291-4300, doi:10.1021/acs.jctc.1c00302 (2021).

Figure 1

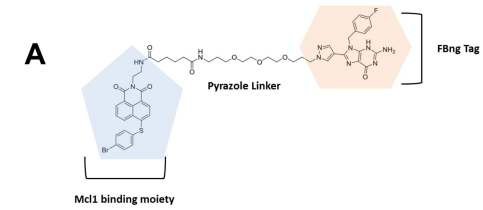

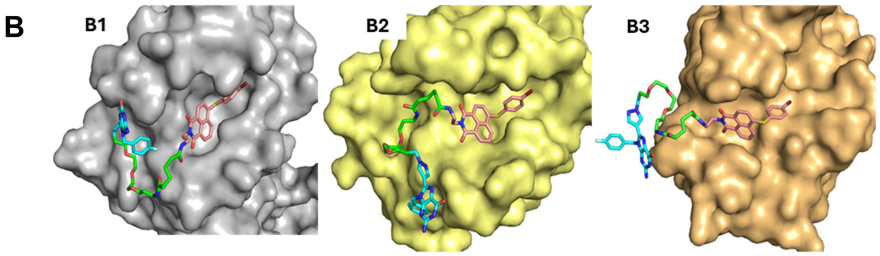

Table 1. Binding energetics and degradation-tag accessibility of AUTAC in Bcl2 family proteins

Complex	ΔG_ Bind	ΔG_ VdW	ΔG_ Electrostatic	FBnG_free (Å²)	FBnG_bound (Å²)	FBnG exposure (%)
AUTAC-Mcl1	-90.91	-62.26	-28.72	542.767	419.014	77.2
AUTAC-Bcl2	-60.26	-51.52	-26.54	533.387	293.690	55.1
AUTAC-Bclxl	-53.41	-53.88	-6.32	548.02	249.95	45.6

Energies (ΔG, kcal/mol) are decomposed into van der Waals (ΔG_vdW) and electrostatic (ΔG_electrostatic) contributions. Solvent-accessible surface area (SASA) of the FBnG degradation tag was calculated in the free state and in the protein-bound complex using identical surface parameters. FBnG exposure is reported as the fraction of free-state SASA retained upon binding.

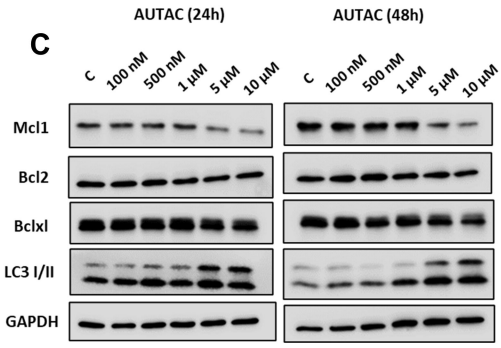

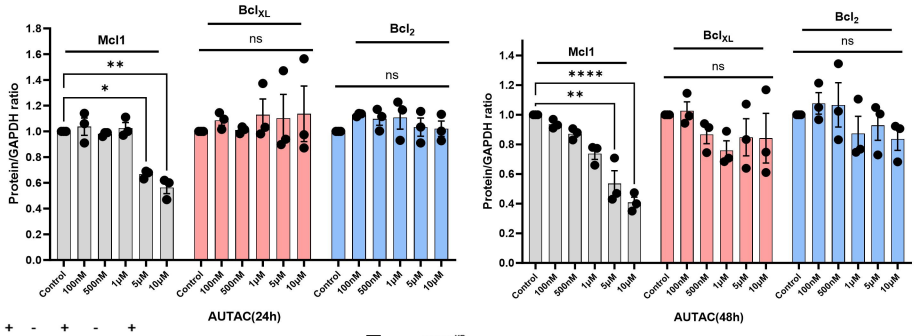

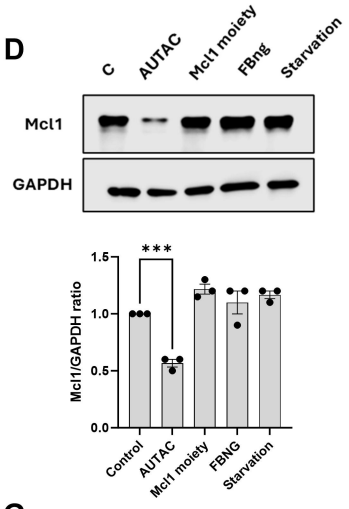

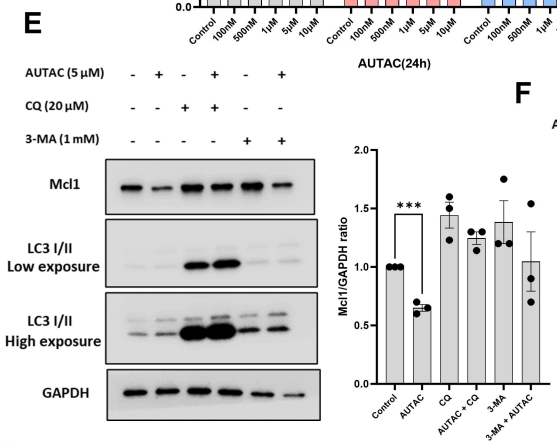

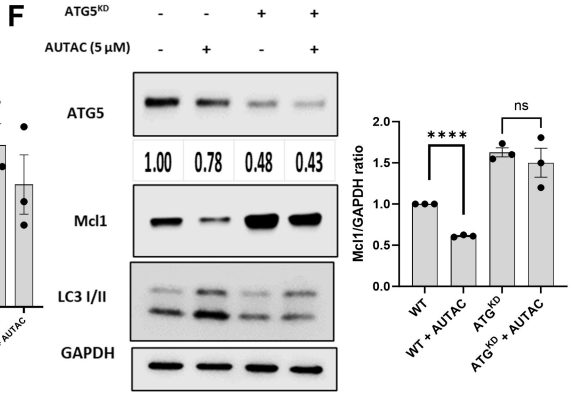

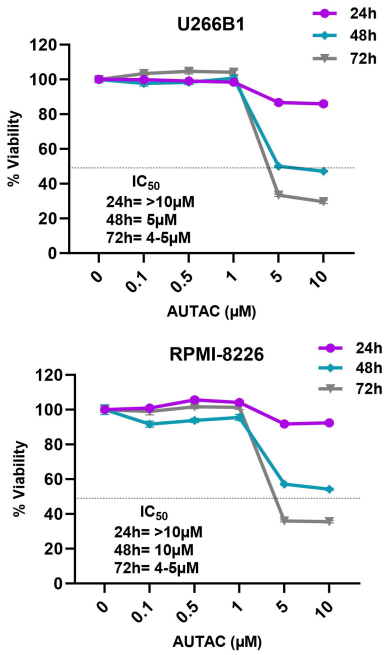

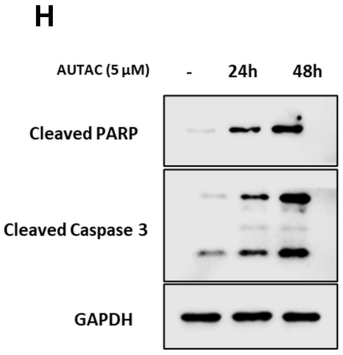

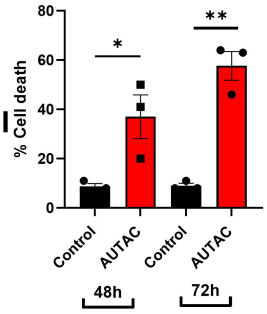

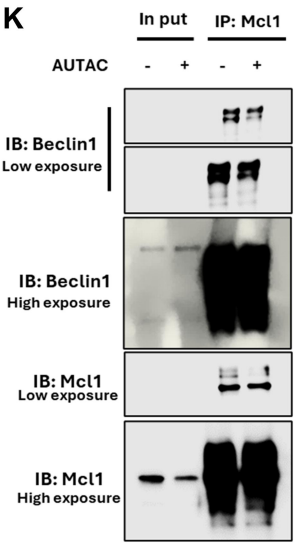

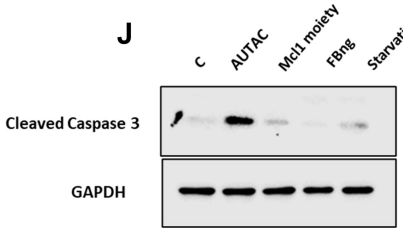

Figure 2

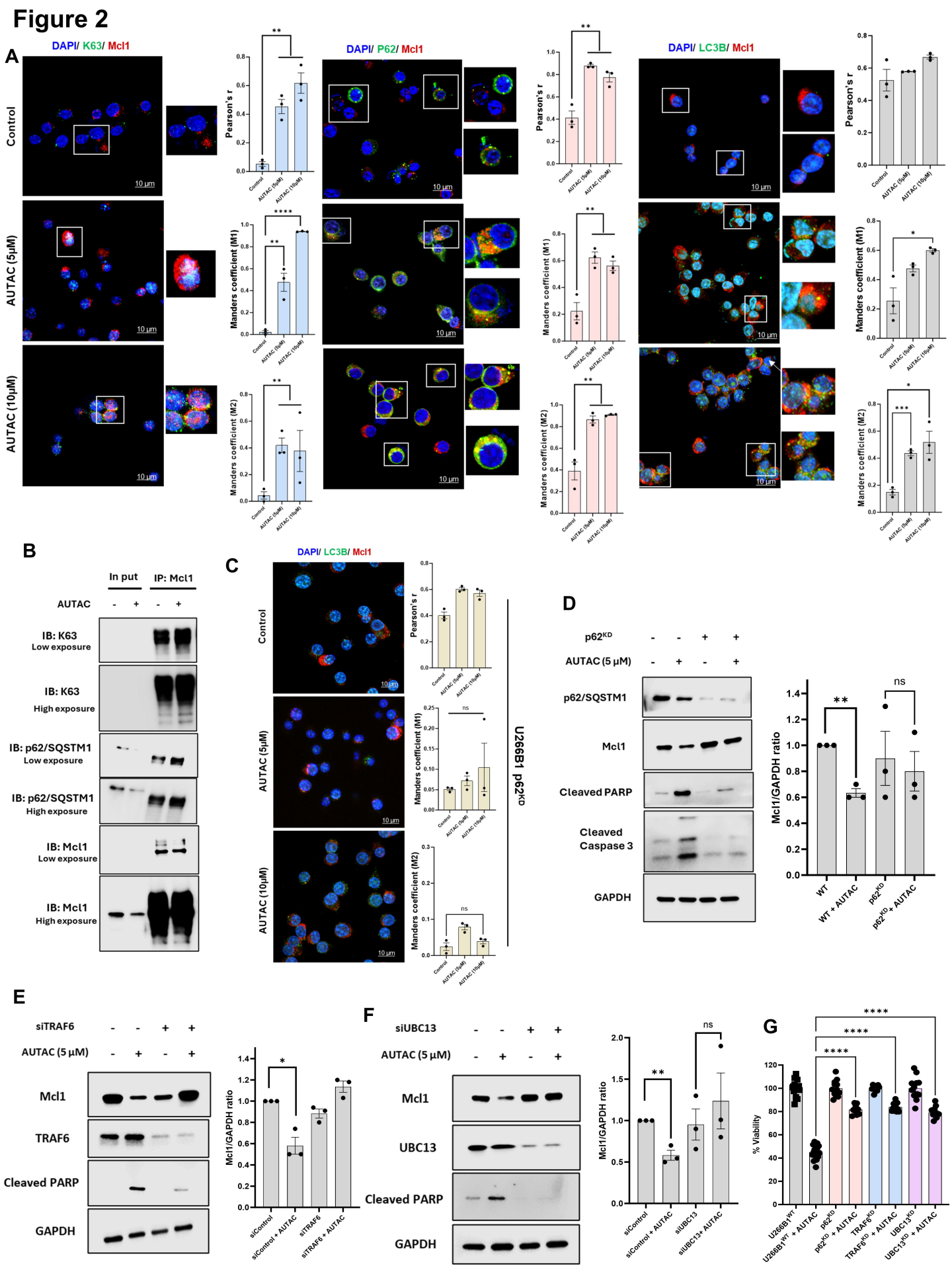
A
DAPI/ K63/ Mcl1
DAPI/ P62/ Mcl1
DAPI/ LC3B/ Mcl1
Control
AUTAC (5μM)
AUTAC (10μM)
10 μm
Pearson's r
Manders coefficient (M1)
Manders coefficient (M2)
Control
AUTAC (5μM)
AUTAC (10μM)
B
In put
IP: Mcl1
AUTAC
IB: K63
Low exposure
IB: K63
High exposure
IB: p62/SQSTM1
Low exposure
IB: p62/SQSTM1
High exposure
IB: Mcl1
Low exposure
IB: Mcl1
High exposure
C
DAPI/ LC3B/ Mcl1
Control
AUTAC (5μM)
AUTAC (10μM)
U266B1 p62KD
D
p62KD
AUTAC (5 μM)
p62/SQSTM1
Mcl1
Cleaved PARP
Cleaved Caspase 3
GAPDH
Mcl1/GAPDH ratio
WT
WT + AUTAC
p62KD
p62KD + AUTAC
E
siTRAF6
AUTAC (5 μM)
Mcl1
TRAF6
Cleaved PARP
GAPDH
siControl
siControl + AUTAC
siTRAF6
siTRAF6 + AUTAC
F
siUBC13
AUTAC (5 μM)
Mcl1
UBC13
Cleaved PARP
GAPDH
siUBC13
siUBC13+ AUTAC
G
% Viability
U266B1WT
U266B1WT + AUTAC
p62KD
p62KD + AUTAC
TRAF6KD
TRAF6KD + AUTAC
UBC13KD
UBC13KD + AUTAC

Figure 3

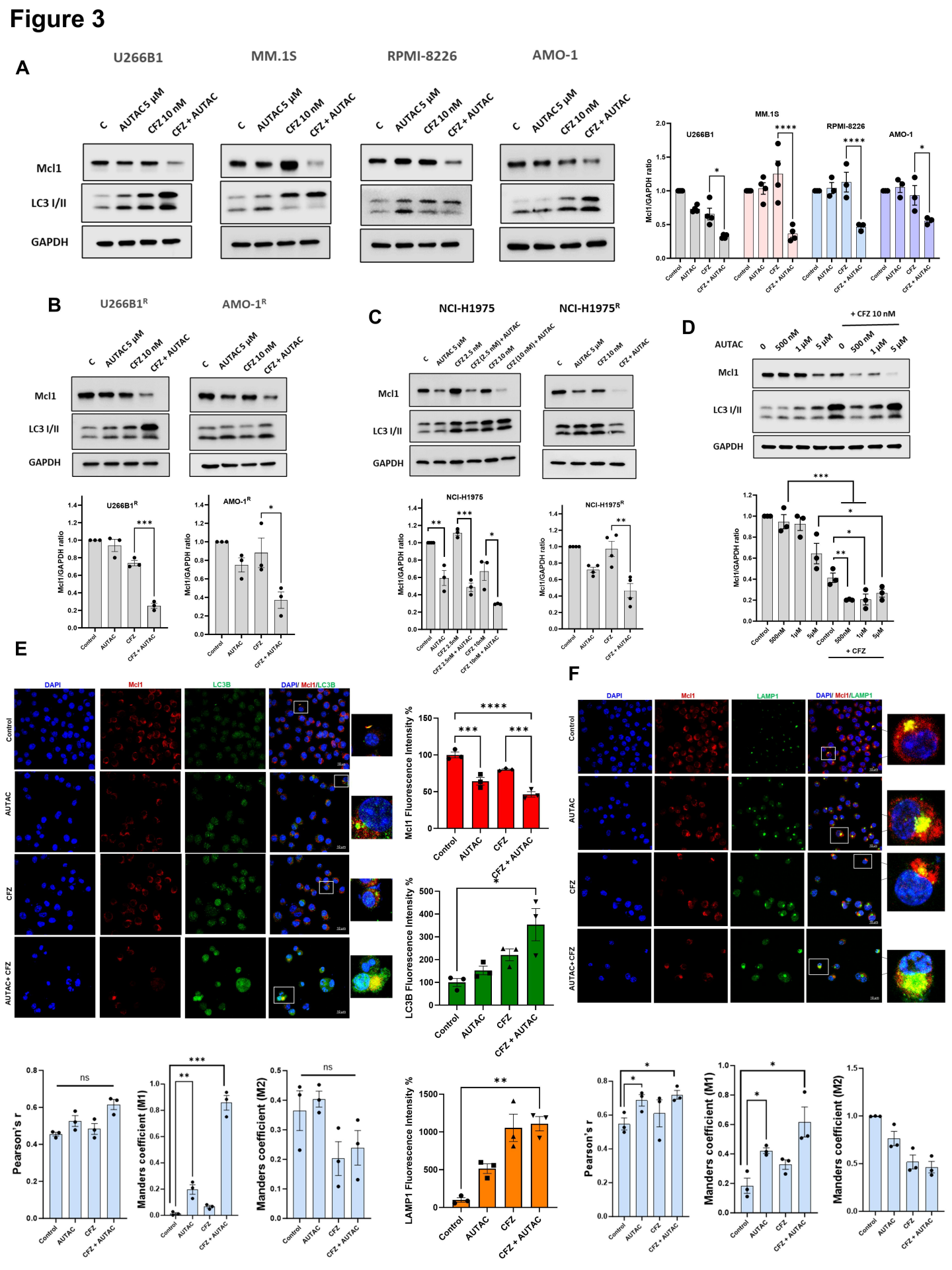
A
U266B1
MM.1S
RPMI-8226
AMO-1
C
AUTAC 5 μM
CFZ 10 nM
CFZ + AUTAC
Mcl1
LC3 I/II
GAPDH
Mcl1/GAPDH ratio
Control
AUTAC
CFZ
CFZ + AUTAC
B
U266B1R
AMO-1R
C
NCI-H1975
NCI-H1975R
CFZ 2.5 nM
CFZ (2.5 nM) + AUTAC
CFZ 10 nM
CFZ (10 nM) + AUTAC
D
+ CFZ 10 nM
AUTAC
0
500 nM
1 μM
5 μM
E
DAPI
Mcl1
LC3B
DAPI/ Mcl1/LC3B
Mcl1 Fluorescence Intensity %
LC3B Fluorescence Intensity %
F
LAMP1
DAPI/ Mcl1/LAMP1
LAMP1 Fluorescence Intensity %
Pearson's r
Manders coefficient (M1)
Manders coefficient (M2)
ns

Figure 4

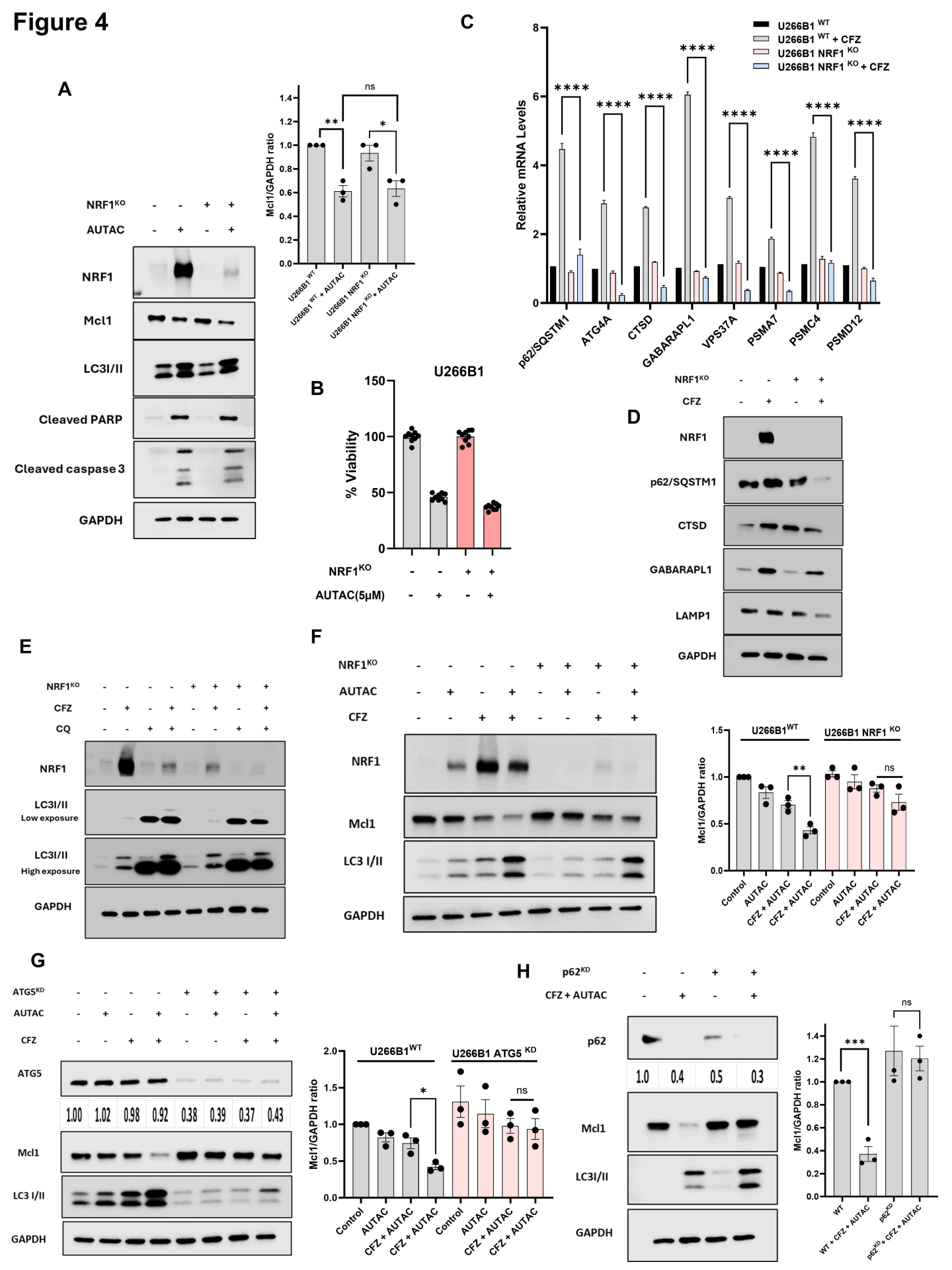
A
NRF1KO - - + +
AUTAC - + - +
NRF1
Mcl1
LC3I/II
Cleaved PARP
Cleaved caspase 3
GAPDH
Mcl1/GAPDH ratio
ns
**
*
U266B1 WT
U266B1 WT + AUTAC
U266B1 NRF1 KO
U266B1 NRF1 KO + AUTAC
B
U266B1
% Viability
NRF1KO - - + +
AUTAC(5μM) - + - +
C
U266B1 WT
U266B1 WT + CFZ
U266B1 NRF1 KO
U266B1 NRF1 KO + CFZ
Relative mRNA Levels
****
p62/SQSTM1
ATG4A
CTSD
GABARAPL1
VPS37A
PSMA7
PSMC4
PSMD12
D
NRF1KO - - + +
CFZ - + - +
NRF1
p62/SQSTM1
CTSD
GABARAPL1
LAMP1
GAPDH
E
NRF1KO - - - - + + + +
CFZ - + - + - + - +
CQ - - + + - - + +
NRF1
LC3I/II
Low exposure
LC3I/II
High exposure
GAPDH
F
NRF1KO - - - - + + + +
AUTAC - + - + - + - +
CFZ - - + + - - + +
NRF1
Mcl1
LC3 I/II
GAPDH
U266B1WT
U266B1 NRF1 KO
Mcl1/GAPDH ratio
**
ns
Control
AUTAC
CFZ + AUTAC
G
ATG5KD - - - - + + + +
AUTAC - + - + - + - +
CFZ - - + + - - + +
ATG5
1.00 1.02 0.98 0.92 0.38 0.39 0.37 0.43
Mcl1
LC3 I/II
GAPDH
U266B1WT
U266B1 ATG5 KD
Mcl1/GAPDH ratio
*
ns
H
p62KD - - + +
CFZ + AUTAC - + - +
p62
1.0 0.4 0.5 0.3
Mcl1
LC3I/II
GAPDH
***
ns
WT
WT + CFZ + AUTAC
p62KD
p62KD + CFZ + AUTAC

Figure 5

A

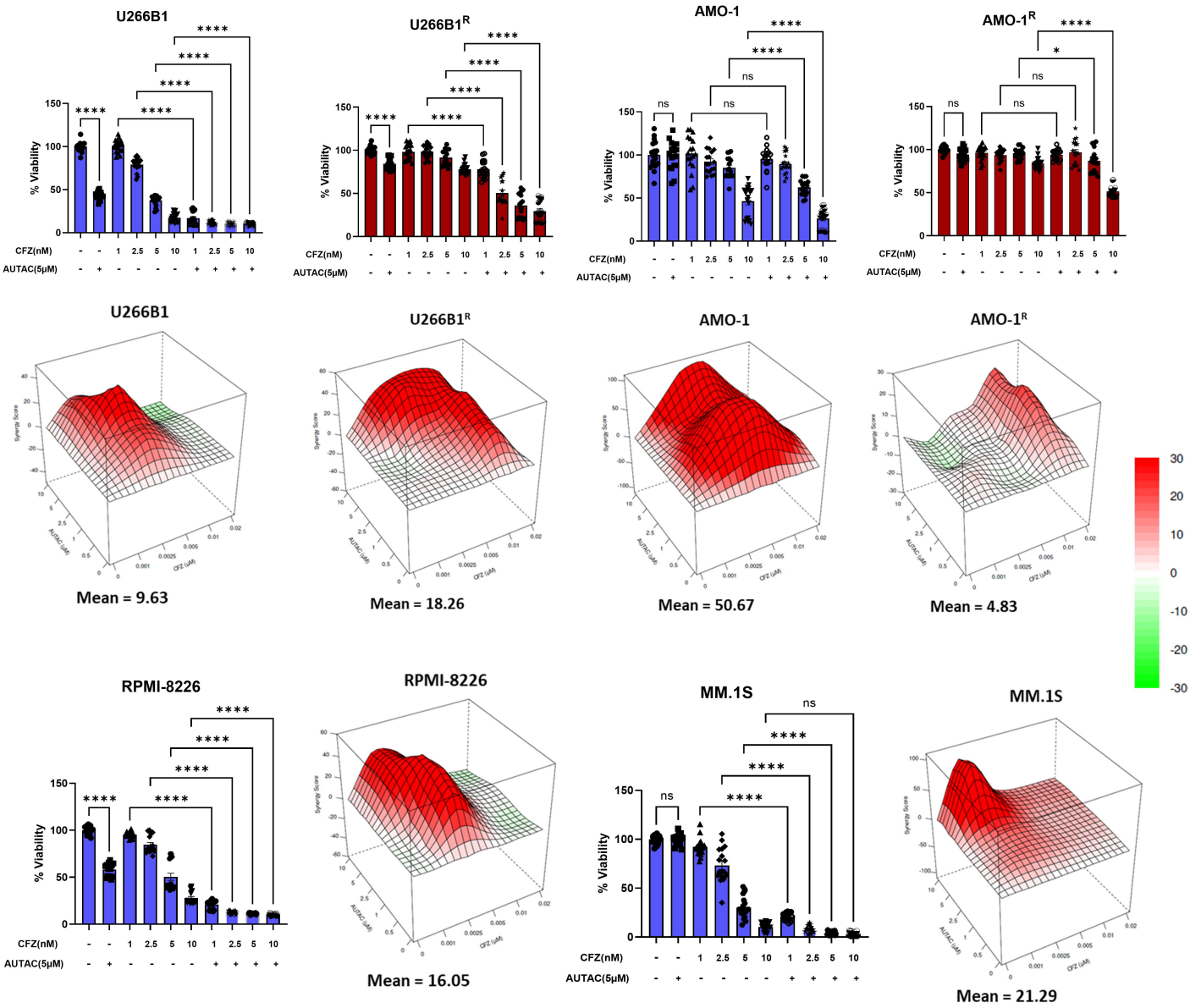
U266B1
U266B1R
AMO-1
AMO-1R
% Viability
CFZ(nM)
AUTAC(5μM)
Mean = 9.63
Mean = 18.26
Mean = 50.67
Mean = 4.83
RPMI-8226
MM.1S
Mean = 16.05
Mean = 21.29

B

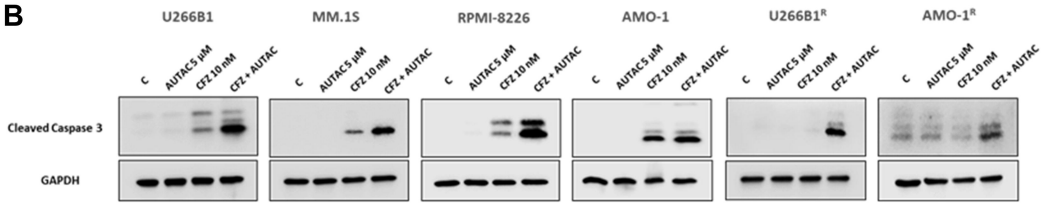
U266B1
MM.1S
RPMI-8226
AMO-1
U266B1R
AMO-1R
C
AUTAC5 μM
CFZ 10 nM
CFZ + AUTAC
Cleaved Caspase 3
GAPDH

C

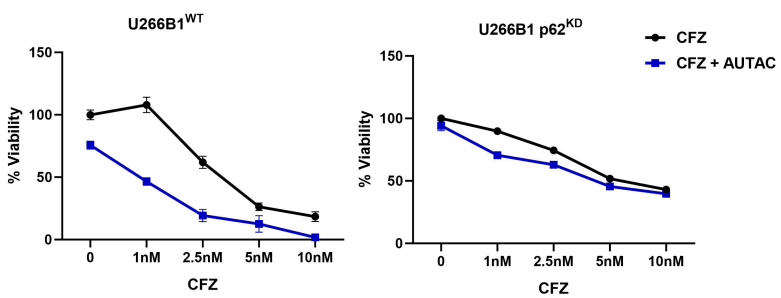
U266B1WT
U266B1 p62KD
CFZ
CFZ + AUTAC
% Viability
0
1nM
2.5nM
5nM
10nM

Figure 6

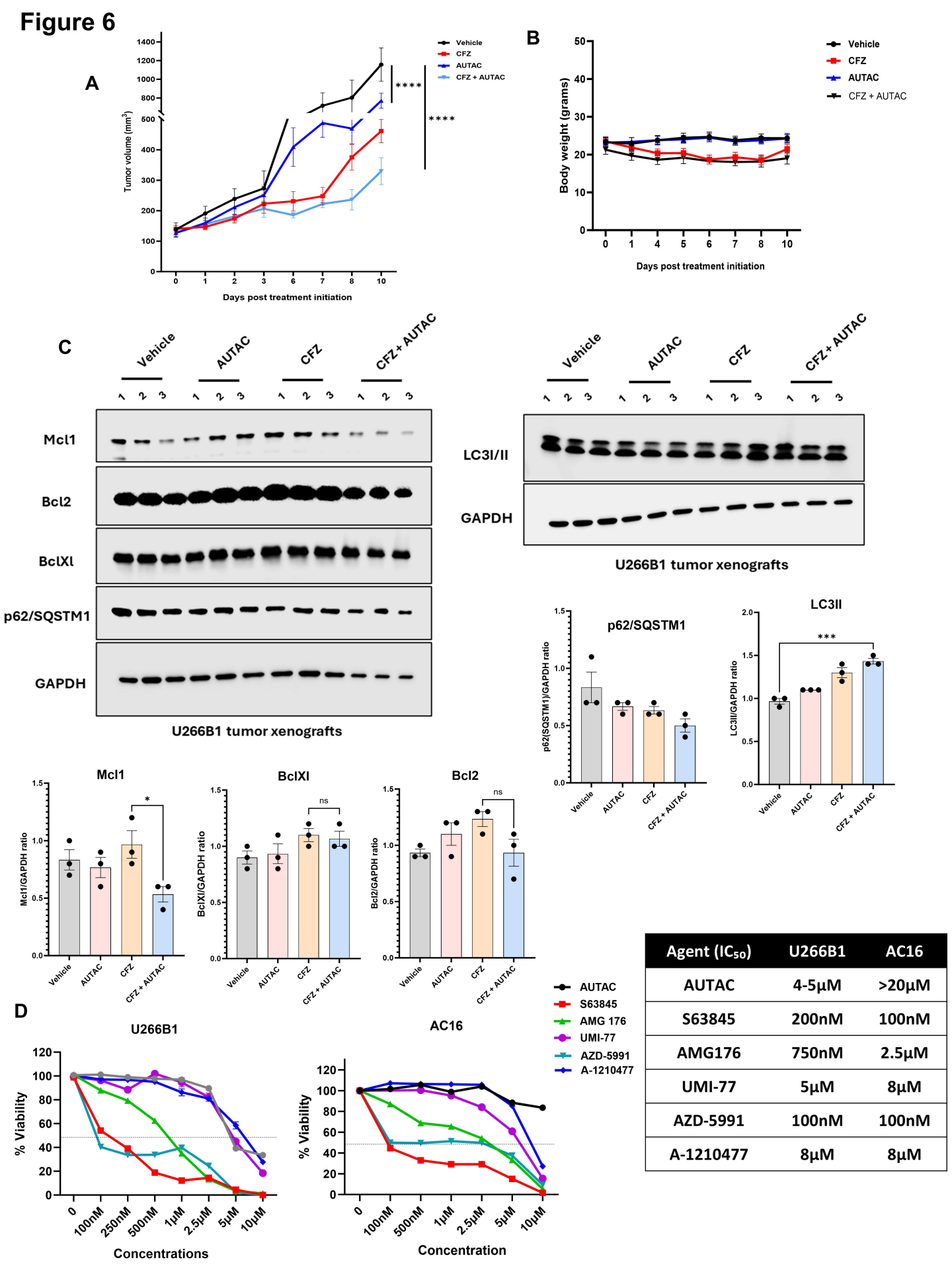

Agent (IC_{50})	U266B1	AC16
AUTAC	4-5µM	>20µM
S63845	200nM	100nM
AMG176	750nM	2.5µM
UMI-77	5µM	8µM
AZD-5991	100nM	100nM
A-1210477	8µM	8µM

Figure 7

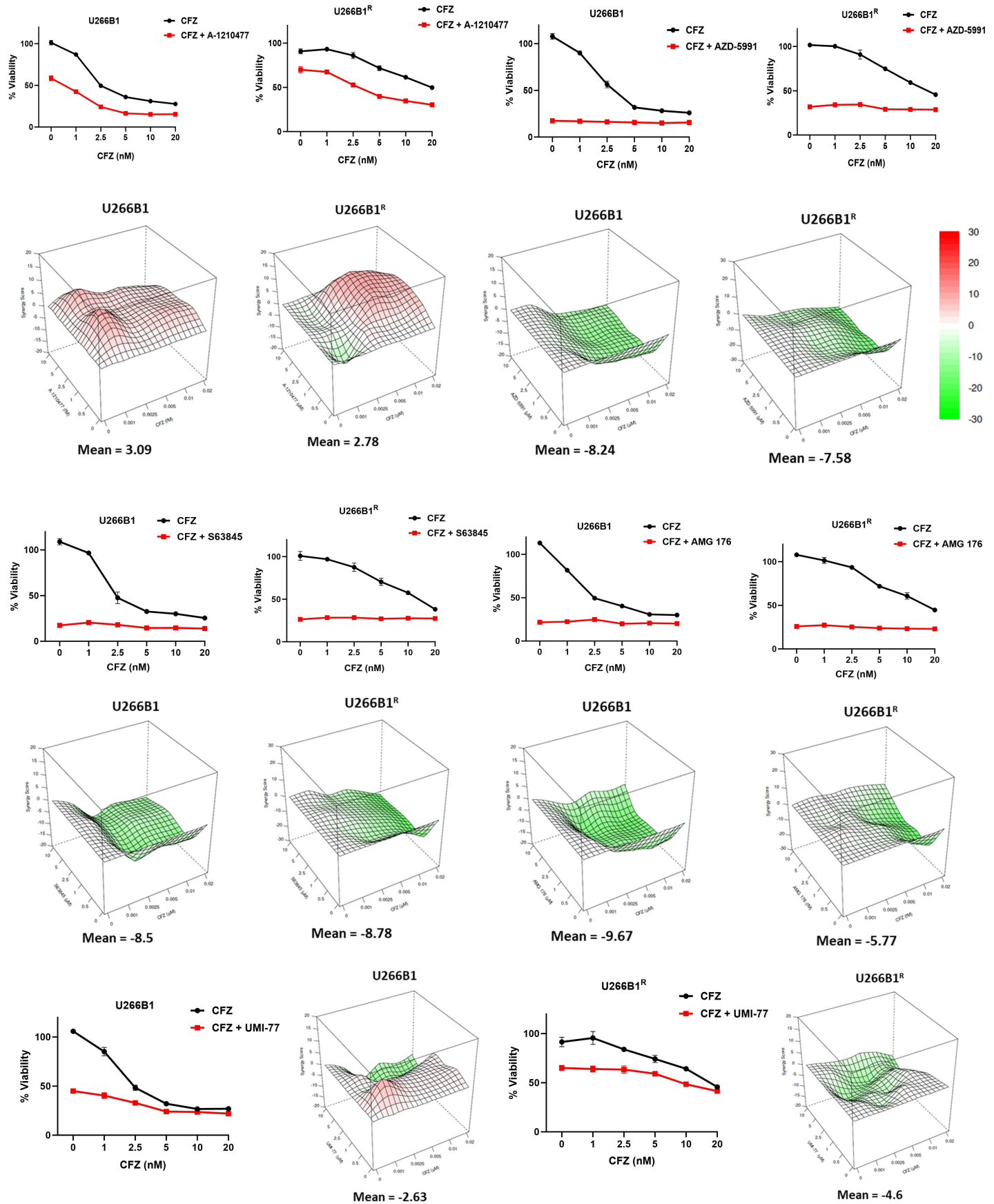
U266B1
CFZ
CFZ + A-1210477
% Viability
CFZ (nM)
U266B1R
CFZ
CFZ + A-1210477
U266B1
CFZ
CFZ + AZD-5991
U266B1R
CFZ
CFZ + AZD-5991
U266B1
Mean = 3.09
U266B1R
Mean = 2.78
U266B1
Mean = -8.24
U266B1R
Mean = -7.58
U266B1
CFZ
CFZ + S63845
U266B1R
CFZ
CFZ + S63845
U266B1
CFZ
CFZ + AMG 176
U266B1R
CFZ
CFZ + AMG 176
U266B1
Mean = -8.5
U266B1R
Mean = -8.78
U266B1
Mean = -9.67
U266B1R
Mean = -5.77
U266B1
CFZ
CFZ + UMI-77
U266B1
Mean = -2.63
U266B1R
CFZ
CFZ + UMI-77
U266B1R
Mean = -4.6

Figure 8

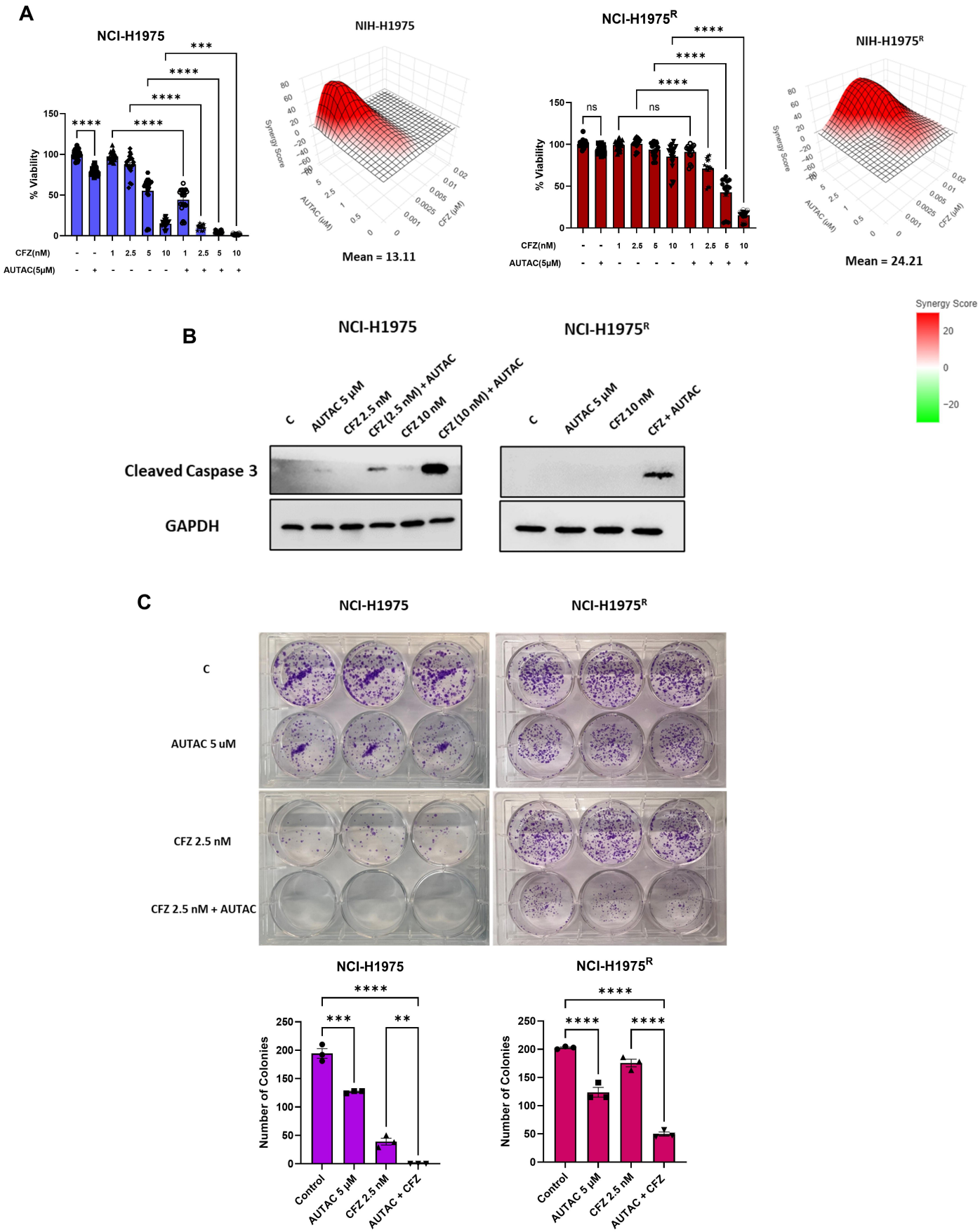
A
NCI-H1975
% Viability
CFZ(nM)
AUTAC(5μM)
NIH-H1975
Synergy Score
AUTAC (μM)
CFZ (μM)
Mean = 13.11
NCI-H1975R
ns
NIH-H1975R
Mean = 24.21
Synergy Score
B
NCI-H1975
NCI-H1975R
C
AUTAC 5 μM
CFZ 2.5 nM
CFZ (2.5 nM) + AUTAC
CFZ 10 nM
CFZ (10 nM) + AUTAC
CFZ + AUTAC
Cleaved Caspase 3
GAPDH
C
NCI-H1975
NCI-H1975R
AUTAC 5 uM
CFZ 2.5 nM
CFZ 2.5 nM + AUTAC
Number of Colonies
Control
AUTAC 5 μM
CFZ 2.5 nM
AUTAC + CFZ